International Journal of Computer Information Systems and Industrial Management Applications
ISSN 2150-7988 Volume 18(16s) 2026 pp. 679-706
https://doi.org/10.70917/ijcisim-2026-4600
Article

Combined Natural Convection and Surface Radiation Heat Transfer from Two Aligned Horizontal Cylinders in a Vented Square Enclosure

Ameen M. Atroshy[1], Omar Mohammed Ali[2]

[1]Engineering Research Center, University of Zakho, Zakho, Iraq
[2]Mechanical Engineering Department, College of Engineering, University of Zakho, Zakho, Iraq
AmeenMustafa98@gmail.com
Omar.Ali@uoz.edu.krd

Abstract: Combined natural convection and surface radiation from two horizontally aligned cylinders at unequal surface temperatures in a vented square enclosure are solved numerically. A two-dimensional turbulent finite-volume model couples the k–ω SST closure with surface-to-surface radiation using ANSYS Fluent Software. The left cylinder is held at a constant lower temperature and the right at a higher, variable one, while a constant inlet velocity at the bottom vent keeps the flow natural-convection-dominated. The model reproduces 18 experimental cases with a mean error of and a maximum of . Sweeps cover Rayleigh numbers from , opening ratios from , spacing ratios from , and surface emissivity from . Emissivity is the controlling parameter. Raising it from increases the total Nusselt number by for the left cylinder and for the right, while the convective contribution changes by less than . Convective transfer peaks near an opening ratio of and at the smallest spacing, whereas the total Nusselt number is highest at the tightest opening, where trapped hot air raises the radiative share. Radiation supplies of the total at and – at unit emissivity, so a convection-only model under-predicts by the same margins. The current arrangement is of significant interest for numerous applications in electronic housings, heat exchangers, and renewable energy fields including solar receiver cavities, flat plate solar collectors, and photovoltaic thermal solar systems.
Keywords: Natural convection, surface-to-surface radiation, vented square enclosure, aligned cylinders, Nusselt number, Rayleigh number, surface emissivity.

1. Introduction

Various techniques exist to improve natural convection heat transfer, including attaching fins to a surface [1], optimizing the geometry of a vented enclosure [2, 3], and placing internal bodies that disturb the flow and enhance heat transfer [4]. Natural convection is especially important in low-power and low-pressure thermal systems, with coupled radiation–convection applications in heat exchangers, building HVAC, electronic cooling, and solar collectors [5]. In vented enclosures, conduction in the solid, natural convection in the fluid, and surface radiation at the walls act together [6, 7], and vent configuration together with internal cylinder placement strongly affects the thermal field [4].

Improving natural convection through surface thermal radiation is a critical aspect of thermal engineering, with wide applications in building HVAC systems, industrial heat exchangers, and electronic device cooling [5]. Passive thermal strategies that couple radiation with natural convection can enhance heat-transfer efficiency and reduce reliance on mechanical heating or cooling [5]. Once the surfaces are even moderately emissive, radiation can carry close to half of the total transfer [5].

These mechanisms govern the performance of several renewable-energy devices. In a solar cavity receiver, the buoyant exchange carries away the concentrated flux that the aperture is intended to retain, so its suppression directly affects the receiver efficiency [8, 9]. In a phase-change storage module the same exchange determines the charging and discharging rate [10]; in the air gap of a flat-plate collector and behind the absorber of a photovoltaic-thermal panel it sets the useful gain and the cell temperature; and in an electronics cabinet, it determines the operating temperature [11]. Silent and maintenance-free operation is more valuable in these applications than the additional capacity that a fan would provide.

Each of the three parameters swept here corresponds to a choice that a designer of such a device makes. The opening ratio is the aperture area of a receiver cavity or the vent area of a storage module, and it is fixed when the housing is built [8, 10]. Inside that housing, the spacing ratio is the pitch of the absorber or heat-exchanger tubes [12, 13]. The surface emissivity is the coating specified for those tubes, and it can be changed after the geometry is fixed, at low cost and without altering the flow path [4, 14]. Determining which of the three controls the total heat transfer, and how much of it radiation carries once the surfaces are no longer polished, is therefore relevant to the selective coatings used on receiver absorbers and to the decision to insulate or to ventilate a storage enclosure [5, 9].

A horizontal cylinder inside a vented enclosure is the canonical element of this class, standing in for absorber tubes inside a receiver cavity, for heat-exchanger tubes, and for heated electronic components. Cavities of this kind are also studied as renewable-energy components in their own right, and a ventilated cavity carrying an internal rotating body has been optimized as the hot side of a thermoelectric generator [15]. Vent-driven through-flow lifts its average Nusselt number well above that of a free-standing cylinder, by 20% to 85% over Rayleigh numbers from 10^3 to 10^6 [16]. The gain survives when a forced inlet drives the cavity into the mixed-convection regime [17, 18]. Opening size determines how much of it is available. A narrow lower vent keeps the cavity buoyancy-driven, while a wide one admits enough momentum to make the flow mixed [16]. Many devices carry two tubes rather than one, and condenser–evaporator pairs run them at different temperatures, so cooling one body and heating its neighbor become a single coupled problem. A second cylinder adds a plume interaction that the opening ratio $O = o/L$ and the spacing ratio $S = s/L$ jointly control [12, 19].

Work on this configuration separates by how many bodies the cavity holds and by whether those bodies share a temperature. Single-body vented studies fix the sensitivity of Nu to opening size and regime, though several of them use a square section rather than a circular one [17, 20]. Outlet placement matters as much as opening size. With the outlet set high on the wall Nu climbs almost linearly with Ri, whereas a central or low outlet drives it down to Ri ≈ 2.5 before it recovers [17]. Two-body vented studies then sweep O and S together at matched conditions, agreeing on Nu rising as the opening widens [12, 19], with the narrower spacings optimal near $S = 0.375$ [19]. Making the inflow and outflow areas unequal is worth a further 10% to 20% [21], and how many vents the cavity carries, and where they sit, weigh as heavily as how large they are [22]. Sealed cavities remove the through-flow and isolate the plume interaction, so the spacing dependence is clearest there. Spacing raises the time-averaged Nu while conduction still dominates and ceases to matter at high Ra [23], and the arrangement of the pair also decides whether the flow remains steady at the highest Ra [24]. Charging the same sealed pair with a CuO-water nanofluid raises Nu with the particle loading, by 0.5% to 5% at loadings up to 1% [25]. Table 1 sets out the studies, their swept ranges in the present notation, and what each reports.

Table 1: Prior studies of convection from one or two horizontal bodies in vented and sealed square enclosures.

Study	Configuration & Medium	Convection mode	Opening & spacing ratios	Parameter ranges	Method	Key finding
Kahwaji et al. (2012) [20]	Vented; one square body	Natural	o = 1, 3 cm (raw opening, not a ratio)	Ra 10^2–6.5×10^5	Numerical, in-house finite-volume-based finite difference, hybrid scheme	Nu peaks at the narrowest enclosure, reaching ≈ 29 against ≈ 17 at the widest
Chamkha et al. (2011) [17]	Vented on the side walls; one square body	Mixed	O = 0.1 (fixed)	Ri 0–10 Re 50–200	Numerical, FDM	Outlet height governs the Ri response: set high, Nu rises almost linearly; set central or low, it falls to Ri ≈ 2.5 before recovering
Ali et al. (2022) [16]	Vented; one cylinder	Natural and mixed	O = 0.2; 0.4; 0.6; 1 (narrow) O = 0.125; 0.25; 0.5; 1 (wide)	Ra 10^3–10^6 Ri 0.1–100	Numerical, FVM	Nu rises with Ra and with opening size, giving 20–85% above a free cylinder

Study	Configuration & Medium	Convection mode	Opening & spacing ratios	Parameter ranges	Method	Key finding
Rahman et al. (2008) [18]	Vented on the side walls; one heat-conducting cylinder, the heat source being a side wall	Mixed	O = 0.1 (fixed)	Ri 0–5 Re 100	Numerical, finite element	Nu on the heated wall rises with Ri, and the best cylinder diameter switches with regime, 0.6 up to Ri 0.75 and 0.4 beyond
Ali and Alomar (2021) [19]	Vented; two cylinders, both heated	Mixed	O = 0.125; 0.375; 1 S = 0.3; 0.375; 0.45	Ri 0.1–20 Re 50–400	Numerical, FVM	Nu rises with Ri, Re and O apart from two exceptions the paper reports itself, at Re = 50 and at full opening; spacing is optimal at S = 0.375
Ali (2022) [12]	Vented; two cylinders, both heated	Natural	O = 0.125; 0.375; 0.625; 1 S = 0.3; 0.375; 0.45	Ra 10^3–10^7	Numerical, FVM	Nu rises with Ra, O and S; +50–100% at low Ra against +20–30% at high Ra, with S saturating by 0.45
Alomar et al. (2023) [21]	Vented; two cylinders, both heated, unequal vents	Mixed	O = 0.125; 0.25 (inflow) O = 0.125 (outflow) S = 0.3; 0.375; 0.45	Ri 0.1–20 Re 50–400	Numerical, FVM	Unequal inflow and outflow areas lift Nu by about 20% at Ri ≤ 1 and about 10% at high Ri; the two cylinders differ by about 11%
Ali and Jalal (2020) [22]	Vented; two cylinders, both heated, vent count varied	Natural	0.2 of the wall height, as one port or two of 0.1 (side walls; the source's own ratio, not O) S = 0.30; 0.35; 0.40; 0.45; 0.50	Ra 10^4; 10^5; 10^6	Numerical, finite element	At constant total open area, the number and placement of the ports control Nu: the symmetric layout leads by about 7% at Ra 10^6, and the ranking reverses at Ra 10^4
Karimi et al. (2016) [13]	Vented on the side walls; two cylinders, both heated; water	Mixed	O = 0.1 (fixed) S = 0.3; 0.4; 0.5 (rises with D; the source fixes the surface gap, not	Ri 0–10 Re 50–200	Numerical, FVM	Nu rises with Ri and with body size, roughly doubling from D = 0.1 to D = 0.3

Study	Configuration & Medium	Convection mode	Opening & spacing ratios	Parameter ranges	Method	Key finding
			the center spacing)			
Al-Omar and Ali (2023) [26]	Vented; two cylinders, hot and cold	Mixed	O = 0.125; 0.375; 1 S = 0.3; 0.375; 0.45	Ri 0.1–20 Re 50–400	Numerical, FVM	Hot-cylinder Nu rises and cold-cylinder Nu falls with Ri, Re and O; the largest single gain across the Ri sweep is 38.1% at O = 0.125 with S = 0.375
Alomar et al. (2024) [27]	Vented; two cylinders, hot and cold	Natural	O = 0.146; 0.439; 1 S = 0.351; 0.439; 0.526	Ra 10^5–3.4×10^6	Experimental	Peak improvement of 30–50% at O = 0.439 with S = 0.351; the validation dataset for the present model
Park et al. (2012) [28]	Sealed; two cylinders, hot and cold	Natural	S = 0.5 (fixed)	Ra 10^3–10^6	Numerical, immersed boundary	The flow reaches a steady state at every Ra; moving the horizontally aligned pair off the mid-plane raises the enclosure-averaged Nu at Ra 10^3 and 10^4, and convection breaks that symmetry above them
Cho et al. (2017) [24]	Sealed; two cylinders, both heated	Natural	S = 0.30; 0.40; 0.50; 0.60; 0.70	Ra 10^3–10^6	Numerical, immersed boundary	Steady to Ra 10^5, and unsteady at 10^6 only at the smallest spacing; widening the spacing raises the cylinder-surface Nu by about 12.8%
Karimi et al. (2014) [23]	Sealed; two cylinders, both heated; water	Natural	S = 0.30; 0.40; 0.50; 0.60	Ra 10^3–10^7	Numerical, FVM	Spacing raises the time-averaged Nu while conduction dominates, then ceases to matter above Ra 10^6 on the paper's own figures, where its abstract and conclusion instead give 10^4 and 10^5
Yousif et al. (2025) [25]	Sealed; two cylinders, both heated; CuO-water nanofluid	Natural	S = 0.30; 0.375; 0.45	Ra 10^3–10^8 volume fraction 0–20%	Numerical, FVM, SIMPLE	Nu rises monotonically with Ra and with particle loading, gaining 0.5–5% over water at loadings to 1%; the spacing trend is not monotonic and reverses at some Ra

Two limits of this body of work carry over to the present problem. Every entry in Table 1 is convection-only, so not one of them reports a convective and a radiative Nusselt number separately. The differentially heated pair fares little better: the configuration of a condenser–evaporator arrangement reduces to a single validated mixed-convection benchmark [26], one experimental natural-convection dataset [27], and one sealed cavity [28]. Spacing and opening are therefore well characterized, and the thermal asymmetry between two bodies is not.

Neglecting radiation is defensible only while the surfaces stay dark. Convective transfer scales with the temperature difference $T_s - T_{ref}$, whereas radiative exchange scales as $\varepsilon\sigma(T_s^4 - T_{ref}^4)$ through view factors between the participating surfaces, so the radiative share climbs with emissivity and with absolute temperature until it rivals the convective share [5]. One consequence is easy to miss: as emissivity rises the convective Nusselt number need not fall, but may hold nearly flat or even increase, while the radiative part lifts the total [2, 29]. Studies that couple the two modes are collected in Table 2.

Table 2: Prior studies of combined natural convection and surface radiation in cavities and cylinder-in-enclosure configurations.

Study	Geometry and internal body	Surface emissivity	Rayleigh number	Radiation model	Method	Key finding
Ali and Mahmood (2020) [4]	Vented square; one heated cylinder	0–1	10^3–10^6	S2S	Numerical, FVM, SIMPLE	Convective Nu is nearly independent of ε while radiative and total Nu rise with it; over ε = 0.2 to 1 the total Nu gains 70–300% at low Ra and 25–125% at high Ra
Prasad et al. (2018a) [2]	Top-open rectangular cavity of aspect ratio 2, vented at the top of the right wall; two heat sources flush with the walls	0.05–0.95	1.075×10^6 (the single value every result is computed at)	Radiosity method	Numerical, finite-volume-based finite difference, stream function–vorticity	The radiative share grows from about 5% to between 32% and 60% as ε rises, depending on where the source sits, with convective Nu near-flat and radiative Nu near-linear in ε
Prasad et al. (2018b) [3]	Right-side open square cavity; heated left wall	0.05–0.95	10^5 (the single value every result is computed at)	Radiosity method	Numerical, finite-volume-based finite difference, stream function–vorticity	Radiative transfer matches convective at high ε; convective Nu falls as radiative Nu rises, and a larger opening raises both
Ridouane et al. (2006) [30]	Sealed square cavity, heated from below and cooled from above; no internal body	0.05; 0.85 (active and insulated walls, set independently)	10^3–2.3×10^6	Radiosity method	Numerical, FDM, ADI with point over-relaxation	Radiation carries more than 60% of the total at ε = 0.85 against about 8% at ε = 0.05

Study	Geometry and internal body	Surface emissivity	Rayleigh number	Radiation model	Method	Key finding
Hinojosa et al. (2005) [31]	Open cavity; heated wall	0; 1	10^3–10^7	Radiosity method	Numerical, FVM, SIMPLEC	Total Nu rises by 93.8–125.7% against the non-radiating case, with radiative Nu about 1.37× the convective
Hamimid and Guellal (2014) [32]	Sealed square cavity; no internal body	0–1	10^4; 10^5; 10^6	Radiosity method	Numerical, FVM, SIMPLER	Convective Nu falls while radiative and total Nu rise with ε; the total roughly doubles at ε = 0.8 and Ra 10^6
Kuznetsov and Nee (2018) [33]	Sealed square cavity; heat source at the top	0.2–0.9	6×10^4–4×10^6	Net radiation method	Numerical, FDM, vorticity-stream function	Radiative Nu rises about 4× across the Ra range while convective Nu stays nearly flat
Sun et al. (2011) [29]	Sealed square cavity; one immersed square body	0; 0.05; 0.1; 1 on the walls (body held at 0.05)	2×10^5–4×10^5	Radiosity method	Numerical, FVM, QUICK, PISO	Surface radiation raises the critical Ra by about 50% and so stabilizes the flow, and convective Nu can rise with ε
Sadaoui et al. (2016) [34]	Sealed shallow rectangular cavity, tilted, with a flat cold cover over a sinusoidal hot absorber heated from below	0–1 (cover, absorber and side walls, separately)	10^3–10^7	Radiosity method	Numerical, control-volume, SIMPLER, QUICK	Radiation raises the total Nu markedly, with convection exceeding radiation at low Ra and the order reversing at high Ra
Sadripour et al. (2017) [35]	Sealed square cavity; corrugated heat source on the floor, circular or rectangular	0.3; 0.9	10^8; 10^{11}	Radiative transfer equation, solved in Fluent	Numerical, FVM, SIMPLEC	Convective Nu falls and radiative Nu rises with ε; circular corrugation improves the radiative transfer at high Ra and rectangular at low Ra
Singh and Singh (2015) [36]	Top-open rectangular cavity of aspect ratio 2; a heat-	0.05–0.85	Ra^* = 4.6×10^5–9.2×10^6 (modified Ra, set by the	Radiosity method	Numerical, FVM, SIMPLE, TDMA	Surface radiation lowers the peak temperature sharply, convective Nu

Study	Geometry and internal body	Surface emissivity	Rayleigh number	Radiation model	Method	Key finding
	generating strip in the conducting left wall		volumetric source rather than a wall temperature)			falling as radiative Nu rises with ε

Radiation therefore changes the total heat transfer by amounts that a convection-only model cannot recover, and the mode split is reported often enough to be treated as standard practice. Several entries come from solar thermal work directly: an inclined sinusoidal solar collector heated from below [34], and an open cavity of the class used to represent a central-receiver aperture [31], a configuration that the same group later analyzed as a receiver [9]. None of the studies in Table 2 includes a second immersed cylinder. Every one of them is an empty cavity, a wall-mounted heat source, or a single immersed body, and only one of them is a vented enclosure that holds a cylinder [4]. That study used a fixed vent geometry, and it treated neither the plume interference between two bodies nor the asymmetry of a hot–cold pair.

Tables 1 and 2 cover the two halves of the present problem separately, and no study covers them together. The convection studies show how O and S govern the flow around an aligned pair. The radiation studies show that surface exchange can dominate the total transfer once the emissivity is appreciable. No published work has combined two aligned cylinders held at different temperatures, a vented square enclosure with O and S both swept, surface-to-surface radiation over a range of emissivity, and convective and radiative Nusselt numbers reported separately for each cylinder. The isolated results cannot be added together, because radiation changes the surface and plume temperatures that drive the buoyant flow, and the flow in turn changes the view factors and the surface temperatures on which radiation depends. The two modes are coupled and must be solved together.

Closing this gap is the purpose of the work reported here. A two-dimensional CFD model based on the Boussinesq approximation, k–ω SST turbulence closure and a surface-to-surface radiation model is applied to two aligned horizontal cylinders in an air-filled vented square enclosure, with C_L held at a constant temperature and C_R at a higher, variable one. Validation uses the experimental measurements of Alomar et al. [27] for the same geometry. Reporting the convective and radiative split on each cylinder, rather than one combined Nusselt number, shows when radiation overtakes convection and how the two bodies share the thermal load. The split also matters in design: the convective share is governed by the vent opening and the internal spacing, both fixed when the enclosure is built, whereas the radiative share is governed by a surface finish that can be specified independently of either. The objectives are:

1. Validate the numerical model against the published experimental measurements of Alomar et al. [27] for C_L and C_R in a vented square enclosure.
2. Determine the combined effects of the opening ratio O, the spacing ratio S, the surface emissivity ε, and the Rayleigh number Ra on the flow topology and the thermal field.
3. Compute the area-averaged convective and radiative Nusselt numbers (Nu_{Conv}, Nu_{Rad}) on C_L and C_R, and quantify the Q_{Conv} to Q_{Rad} partitioning.
4. Identify the geometric and thermal combinations that raise total heat dissipation under coupled convection and radiation.

Section 2 sets out the methodology, Section 3 presents and discusses the results, and Section 4 states the conclusions.

2. Methodology

2.1 Physical Problem and Computational Domain

Two horizontal cylinders of equal diameter D occupy the horizontal mid-plane of a square vented enclosure of side length L. C_L is maintained at the lower surface temperature T_L; C_R is held at the higher surface temperature T_R. Air enters through a bottom vent of width o and exits through an identical top vent on the opposite wall.

The computational domain is geometrically similar to the experimental rig of Alomar et al. [27]. All linear dimensions are scaled by a factor of $200/171$ to produce a 200 mm square enclosure while preserving the opening ratio O, the spacing ratio S, and the diameter ratio $D_r = D/L$. The cylinder diameter in the scaled domain is $D = 33.33$ mm ($D_r = 0.167$). Figure 1 shows the domain geometry.

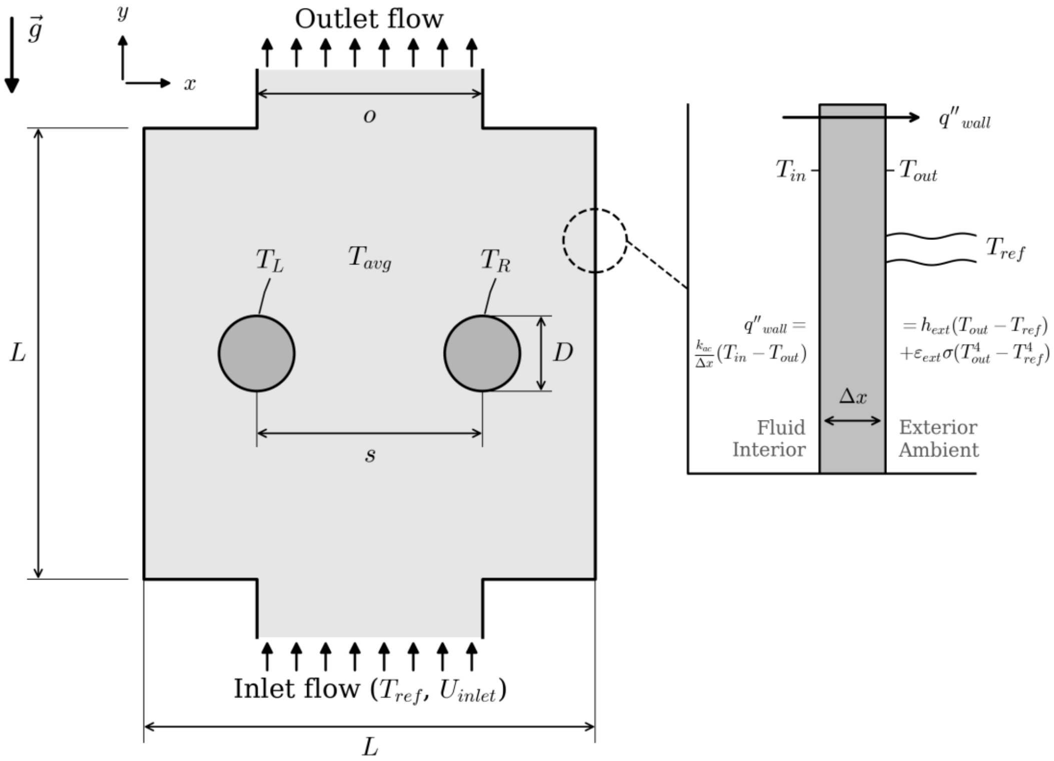

Figure (1): Schematic diagram of the vented enclosure computational domain.

Both cylinders are positioned $s/2$ from the enclosure centerline, keeping the pair centered horizontally. The top and bottom boundaries each consist of solid wall segments flanking the central vent, while the left and right boundaries are fully solid.

The domain is treated as two-dimensional because the experimental rig has a spanwise depth $W_z =$ 370 mm and a cylinder diameter of 28.5 mm, yielding a spanwise depth-to-diameter ratio of ≈ 13. Each cylinder measures 400 mm and runs past the duct walls into end supports, so the flow-bearing span is the shorter of the two. At this aspect ratio, three-dimensional end-wall effects are confined to regions near the lateral faces and do not reach the mid-span plane [37, 38]. Nu trends with respect to O, S, ε, and Ra are well-captured in two dimensions: the cylinder diameter exceeds the conductive boundary-layer thickness at all tested Ra, and the high-aspect-ratio vent geometry suppresses corner vortices that would otherwise break two-dimensional symmetry. The two-dimensional formulation reproduces the reference measurements to within the maximum comparison error reported in Section 3.1.

2.2 Governing Equations and Fluid Properties

The mathematical model assumes the flow is steady, two-dimensional, incompressible, turbulent, and buoyancy-driven. The specific heat capacity (c_p), dynamic viscosity (μ), and thermal conductivity (k_f) of air are taken as the domain-averaged values reported from the converged CFD solution for each case, while density follows the Boussinesq approximation ($\beta\Delta T \ll 1$) in the buoyancy term. Its validity for air extends to $\Delta T <$ 28.6°C [39], well above the maximum ΔT of 18°C reached in the present study. The Reynolds-Averaged Navier–Stokes (RANS) equations [40] are:

Continuity:

$$\frac{\partial u_i}{\partial x_i} = 0 \qquad (1)$$

Momentum:

$$\rho_0 \frac{\partial (u_i u_j)}{\partial x_j} = -\frac{\partial P}{\partial x_i} + \frac{\partial}{\partial x_j}\left[(\mu + \mu_t)\left(\frac{\partial u_i}{\partial x_j} + \frac{\partial u_j}{\partial x_i}\right)\right] + \rho_0 g_i \beta (T - T_{ref}) \qquad (2)$$

Energy:

$$\rho_0 c_p \frac{\partial(u_j T)}{\partial x_j} = \frac{\partial}{\partial x_j}\left[\left(k_f + \frac{c_p \mu_t}{Pr_t}\right)\frac{\partial T}{\partial x_j}\right] - \nabla \cdot q_{Rad} \qquad (3)$$

where μ_t is the turbulent viscosity, Pr_t is the turbulent Prandtl number, and $\nabla \cdot q_{Rad}$ is the radiative source term. Air is treated as a non-participating medium in Section 2.3, so this term vanishes inside the fluid and radiation enters the solution through the surface energy balance at the cylinder and enclosure walls.

Turbulence Model. Turbulence is closed with the Shear Stress Transport (SST) k–ω model [41]. The SST formulation resolves the viscous sublayer near walls and blends to k–ε behavior in the free stream, a combination suited to buoyancy-driven flows where steep wall-normal gradients coexist with free-stream separation in the cylinder wake. Two precedents in this geometry set the choice. The experiment used for comparison here reports its own measurements under steady, turbulent and incompressible flow conditions [27], so a turbulent treatment matches the regime the reference data were taken in. The closest prior numerical study, a single cylinder in the same vented square enclosure over Ra from 10^3 to 10^6, likewise solved the field with a k–ω closure rather than a laminar formulation [16]. The SST variant is preferred here over the standard form because it integrates to the wall, and a low-Reynolds-number closure of this type returns the laminar solution wherever turbulence production vanishes. One closure therefore spans the whole sweep without switching formulation between the conduction-controlled cases at low Ra and the plume-driven cases at high Ra, and it captures the steep near-wall temperature gradients and free-stream wake separation that intensify with the buoyant plume at the upper end of the range. The transport equations for turbulent kinetic energy k and specific dissipation rate ω, including the standard transformation for buoyancy production terms [42], are:

$$\frac{\partial}{\partial x_j}(\rho u_j k) = \frac{\partial}{\partial x_j}\left[\left(\mu + \frac{\mu_t}{\sigma_k}\right)\frac{\partial k}{\partial x_j}\right] + G_k - Y_k + G_b \qquad (4a)$$

$$\frac{\partial}{\partial x_j}(\rho u_j \omega) = \frac{\partial}{\partial x_j}\left[\left(\mu + \frac{\mu_t}{\sigma_\omega}\right)\frac{\partial \omega}{\partial x_j}\right] + G_\omega - Y_\omega + G_{\omega b} + D_\omega \qquad (4b)$$

A production limiter prevents excessive turbulence build-up at cylinder stagnation zones. The near-wall mesh maintains $y^+ \leq 1$ on all solid surfaces.

Four dimensionless groups characterize the flow regime. Gr quantifies buoyancy-driven convection relative to viscous resistance, with the enclosure side length L as the characteristic length:

$$Gr = \frac{g\beta\Delta T L^3}{\nu^2} \qquad (5)$$

where $g = 9.81$ m/s^2 is gravitational acceleration, $\Delta T = T_R - T_L$ is the temperature difference between the two cylinder surfaces, $\beta = 2/(T_L + T_R)$ is the thermal expansion coefficient of air (temperatures in kelvin), and $\nu = \mu/\rho$ is the kinematic viscosity, all taken as the domain-averaged values of the converged solution. In the parametric study, Gr (and hence Ra) is varied by adjusting T_R while T_L is held fixed. Ra follows directly from Gr through the Prandtl number:

$$Ra = Gr \cdot Pr = \frac{g\beta\Delta T L^3}{\nu\alpha} \qquad (5a)$$

where $Pr = \mu c_p/k_f$ is the Prandtl number and $\alpha = k_f/(\rho c_p)$ is the thermal diffusivity of air. Re characterizes the inertia of the inlet flow at the lower vent relative to viscous resistance, with the lower vent width o as the characteristic length:

$$Re = \frac{U_{inlet}\, o}{\nu} \qquad (6)$$

Ri expresses the ratio of buoyancy to inertial forcing through Gr and Re and is the primary regime indicator for mixed convection:

$$Ri = \frac{Gr}{Re^2} \qquad (7)$$

At $Ri \gg 1$ buoyancy dominates and the flow is natural-convection-controlled; at $Ri \ll 1$ forced convection regulated by the inlet vent governs; at $Ri \sim 1$ both modes contribute comparably. The inlet velocity is set so that the flow remains natural-convection-controlled in every case.

2.3 Thermal Radiation Modeling

The Surface-to-Surface (S2S) radiation model is selected because air at atmospheric pressure is a non-participating medium (optical thickness $\tau \ll 0.1$) [43]. Gray-diffuse surfaces, no participating medium and view factor closure ($\sum F_{ij} = 1$) are assumed. The radiosity J_i of surface i is:

$$J_i = \varepsilon_i \sigma T_i^4 + \rho_i \sum_{j=1}^{N} F_{ij} J_j \quad (8)$$

View factors F_{ij} are computed over the enclosure surfaces, so that the geometric occlusion between the two cylinders is captured. An external ambient radiation temperature of 35°C is specified at the vent openings.

2.4 Boundary Conditions

Cylinders. Both cylinder surfaces impose no-slip walls with fixed temperatures:

$$C_L:\ u_i = 0,\ T = T_L \quad (9)$$

$$C_R:\ u_i = 0,\ T = T_R \quad (10)$$

In the S2S model, both cylinder surfaces are treated as gray-diffuse radiators with emissivity ε_c. The validation cases (Section 3.1) adopt a literature value of $\varepsilon_c = 0.07$ for the commercial copper cylinders [14], whereas the emissivity sweep (Section 3.5) varies ε_c over $0 \leq \varepsilon_c \leq 1$.

Enclosure Walls. The solid walls are treated as no-slip boundaries with a mixed thermal condition:

$$u_i = 0, \quad q''_{wall} = \frac{k_{acrylic}}{\Delta x}(T_{in} - T_{out}) = h_{ext}(T_{out} - T_{ref}) + \varepsilon_{ext}\sigma(T_{out}^4 - T_{ref}^4) \quad (11)$$

The exterior acrylic face radiates to the ambient as a gray-diffuse surface with emissivity $\varepsilon_{ext} = 0.93$, a literature value for clear acrylic [14]. Equation (11) retains the finite thermal resistance of the acrylic wall through the conjugate condition.

Bottom Vent (Inlet). The lower opening is a velocity inlet with prescribed uniform magnitude U_{inlet} and inlet temperature equal to the ambient reference:

$$u_i = U_{inlet}, \quad T = T_{ref} \quad (12)$$

The opening is treated as a black-body surface in the radiation exchange. U_{inlet} is constant in each case.

Top Vent (Outlet). The upper opening is a pressure outlet at atmospheric pressure:

$$\frac{\partial u_i}{\partial y} = 0, \quad \frac{\partial T}{\partial y} = 0, \quad P_{gauge} = 0 \quad (13)$$

The outlet opening is likewise modeled as a black-body surface.

2.5 Nusselt Number

Heat transport from the cylinder boundaries is partitioned into convective and radiative components. The convective (Nu_{Conv}) and radiative (Nu_{Rad}) Nusselt numbers of each cylinder are formed from the heat fluxes q''_{Conv} and q''_{Rad} averaged over its full perimeter:

$$Nu_{Conv} = \frac{q''_{Conv} D}{(T_s - T_{avg})k_f}, \quad Nu_{Rad} = \frac{q''_{Rad} D}{(T_s - T_{avg})k_f} \quad (14a)$$

Both are therefore area-averaged quantities, and the total follows from the superposition of the two modes:

$$Nu_{Tot} = Nu_{Conv} + Nu_{Rad} \quad (14b)$$

In these formulations, T_s denotes the constant cylinder surface temperature and T_{avg} is the volume-averaged temperature of the air inside the enclosure, computed from the CFD solution at each parametric case. The enclosure-averaged temperature difference ($T_s - T_{avg}$) is adopted as the driving potential because it accounts for the stratified thermal field that develops between C_L and C_R, where a fixed ambient reference would overestimate the effective temperature gradient seen by each surface.

2.6 Numerical Solution

The governing equations are solved using the pressure-based finite-volume method in ANSYS Fluent 2026 R1 (2D planar). Pressure–velocity coupling is handled by the SIMPLE algorithm. Second-order upwind schemes are applied to momentum, energy, k, and ω. Gradients are computed with the Least Squares Cell Based method, and pressure interpolation uses the Body Force Weighted scheme suited to buoyancy-driven flow.

Convergence is assessed by monitoring scaled residuals (10^{-6} for energy, 10^{-4} for continuity, momentum, and turbulence) and the stabilization of Nu on C_L and C_R. The radiation field is updated every 10 iterations with a maximum of 100 radiation iterations per cycle and a residual criterion of 10^{-4}.

2.7 Grid Independence

A grid-independence study was conducted focusing on the baseline operating point of a parametric investigation with parameters set to $\varepsilon = 0.5$, $O = 0.5$, $S = 0.5$, and $Ra = 3.37 \times 10^6$. The analysis involved thirteen quadrilateral-dominant meshes with element counts ranging from 3246 to 192485. The study specifically assessed the impact of mesh size on the convection and radiation-averaged Nusselt number (Nu) along each circular cylinder, ensuring that the near-wall layers were clustered appropriately to maintain a wall y^+ value of ≤ 1.

Table 3: Grid-independence study at the baseline operating point (ε = 0.5, O = 0.5, S = 0.5, Ra = 3.37 × 10^6): mesh size, area-averaged Nusselt numbers on C_L and C_R, and mesh-quality metrics.

Mesh	Nodes	Elements	Convective Nusselt number of C_L	Radiative Nusselt number of C_L	Convective Nusselt number of C_R	Radiative Nusselt number of C_R	Orthogonal quality	Orthogonal skewness
Mesh 1	3362	3246	6.296	3.912	6.673	4.146	0.9461	0.1706
Mesh 2	3788	3708	6.315	3.911	6.683	4.154	0.9555	0.0894
Mesh 3	4588	4439	6.327	3.917	6.685	4.154	0.9564	0.1495
Mesh 4	5668	5511	6.335	3.920	6.694	4.158	0.9566	0.1414
Mesh 5	7636	7406	6.342	3.925	6.700	4.158	0.9604	0.1396
Mesh 6	11066	10753	6.349	3.926	6.726	4.155	0.9726	0.1328
Mesh 7	**19207**	**18734**	**6.362**	**3.938**	**6.733**	**4.158**	**0.9824**	**0.0964**
Mesh 8	35657	35047	6.360	3.938	6.740	4.158	0.9878	0.0818
Mesh 9	57441	56658	6.366	3.938	6.737	4.159	0.9915	0.0723
Mesh 10	84188	83026	6.363	3.938	6.736	4.159	0.9932	0.0688
Mesh 11	113818	112396	6.364	3.938	6.736	4.158	0.9938	0.0611
Mesh 12	153270	151623	6.362	3.939	6.731	4.159	0.9980	0.0585
Mesh 13	194349	192485	6.362	3.939	6.736	4.159	0.9989	0.0552

Results summarized in Table 3 illustrate how varying mesh sizes influenced the numerical precision of the Nusselt number while keeping other parameters constant. After thorough evaluation, Mesh 7 emerged as the optimal choice for subsequent simulations due to its excellent convergence characteristics and high mesh quality, with an orthogonal quality nearing 1 and orthogonal skewness around 0, leading to reliable Nu results. The discrepancies observed when comparing Mesh 7 to finer meshes were minimal, at less than 1%, thus satisfying the established tolerance criteria. Mesh 7 effectively resolved the boundary layer and offered a favorable balance between accuracy and computational efficiency. Further mesh refinements produced only marginal improvements. In contrast, the coarser meshes (Meshes 1 to 6) exhibited significant discrepancies and poor quality, indicating their inadequate resolution for achieving precise numerical results. Overall, the convergence achieved with Mesh 7 confirmed reliable and consistent outcomes for the Nusselt number under the studied conditions.

3. Results and Discussion

The geometry follows Section 2.1, with diameter ratio $D_r = 0.167$. The temperature of C_R sets the Rayleigh number, so C_R is always hotter than C_L and both surfaces stay above the ambient air temperature. Each effect reported below is isolated about a single common baseline ($O = 0.5$, $S = 0.5$, $\varepsilon = 0.5$, $Ra = 3.37 \times 10^6$) by holding every governing quantity at that baseline and varying only the quantity under study. The governing quantities and the ranges over which they are swept are:

- Ra: $10^3 \le Ra \le 10^7$.
- ε: $0 \le \varepsilon \le 1$.
- S: $0.25 \le S \le 0.75$.
- O: $0.05 \le O \le 1$.

The actions of these variables on Nu_{Conv}, Nu_{Rad}, and Nu_{Tot} of C_L and C_R, together with the temperature and velocity fields inside the enclosure, are presented and discussed in the following subsections. Within each sweep, all contour panels share a common color bar range, so the panels may be compared directly.

3.1 Validation of the present study

The CFD model is benchmarked against the convective heat-transfer measurements of Alomar et al. [27], who tested two horizontal copper cylinders inside an acrylic enclosure at nine S–O configurations spanning $S =$ 0.351, 0.439, and 0.526 with $O = 0.146$, 0.439, and 1.000. Cylinder surface temperatures were recorded by nine DS18B20 digital sensors distributed circumferentially and longitudinally along each cylinder; the enclosure air temperature was measured by three further sensors placed between the cylinders and the enclosure wall; and electrical voltage and current were logged to determine the heat input. Radiation and conduction losses were quantified separately and remained below 1% of the convective heat transfer at every tested condition. Each geometry was tested at five different Rayleigh numbers, giving 45 measured cases in total. The comparison reported below uses 18 of those cases, covering all nine geometries at two of the five Rayleigh numbers of each.

The comparison metric is the pair-averaged convective Nusselt number of Eq. (15), computed independently from the experimental data and from the CFD solution. Both sides use the definition of Eq. (14b): the experimental values are not the Nusselt numbers printed by Alomar et al. [27] but are recomputed here from their reported surface temperatures and heat inputs, with T_{avg} taken from the air temperatures they logged between the cylinders and the enclosure wall and the air properties evaluated from the present converged solution, which the reference does not report. The two sides therefore share the same characteristic length, the cylinder diameter, and the same driving temperature difference, the surface value less the enclosure air value, and the comparison error below measures a difference in predicted heat transfer rather than a difference in data reduction.

$$\overline{Nu}_{avg} = \frac{Nu_{C_L} + Nu_{C_R}}{2} \qquad (15)$$

The comparison error is

$$E = \left| \frac{\overline{Nu}_{exp} - \overline{Nu}_{CFD}}{\overline{Nu}_{exp}} \right| \times 100\% \qquad (16)$$

where $\overline{Nu}_{exp}$ and $\overline{Nu}_{CFD}$ are the experimental and simulated pair-averaged values, respectively. Tables 4 and 5 list $\overline{Nu}_{exp}$, $\overline{Nu}_{CFD}$, and E for the 18 experimental cases, grouped into the lower-Ra and higher-Ra subsets of each geometry.

Table 4: Comparison between the present numerical results and the previous experimental work of Alomar et al. [27], at the lower Ra of each geometry.

Spacing ratio	Opening ratio	Experimental Nusselt number	Predicted Nusselt number	Comparison error (%)
0.351	0.146	6.205	6.575	6.0
0.351	0.439	7.340	7.045	4.0
0.351	1.000	7.000	6.660	4.9

Spacing ratio	Opening ratio	Experimental Nusselt number	Predicted Nusselt number	Comparison error (%)
0.439	0.146	6.600	7.045	6.7
0.439	0.439	6.470	6.780	4.8
0.439	1.000	6.250	6.485	3.8
0.526	0.146	5.675	5.715	0.7
0.526	0.439	6.105	6.500	6.5
0.526	1.000	6.220	6.590	5.9

Table 5: Comparison between the present numerical results and the previous experimental work of Alomar et al. [27], at the higher Ra of each geometry.

Spacing ratio	Opening ratio	Experimental Nusselt number	Predicted Nusselt number	Comparison error (%)
0.351	0.146	6.755	6.985	3.4
0.351	0.439	7.715	7.605	1.4
0.351	1.000	7.380	7.150	3.1
0.439	0.146	7.295	6.940	4.9
0.439	0.439	7.650	7.250	5.2
0.439	1.000	6.600	6.830	3.5
0.526	0.146	6.145	6.575	7.0
0.526	0.439	6.185	6.550	5.9
0.526	1.000	6.500	6.835	5.2

Across the 18 experimental cases, E ranges from 0.7% to 7.0%, with a mean of 4.6%, which is 4.8% for the lower-Ra subset and 4.4% for the higher-Ra subset. The largest deviations, $E \approx 7\%$, occur at the tightest opening, $O = 0.146$, where vent-driven inertia and thermal-plume confinement steepen the near-wall temperature gradients that a two-dimensional, steady formulation resolves with limited fidelity. There are three main reasons for this error. First, the surface emissivity of the cylinders and the enclosure walls was assigned in the model rather than measured on the rig, so the radiative part of the predicted heat transfer is not exact. Second, the inlet air velocity at the lower vent was not measured in the experiment and had to be supplied to the model. Third, the experiment used a small number of temperature sensors at the inlet and outlet openings and for the air inside the enclosure, so these measurements carry a margin of error that passes directly into the experimental Nusselt number. No case exceeds $E = 7.0\%$. The model is therefore applied without correction to the parametric sweeps in Sections 3.2 to 3.5, with the largest residual error at the tightest opening. The validation cases reach $Ra = 3.37 \times 10^6$, so the upper end of the Ra sweep extends beyond the range over which the model has been compared with measurement.

3.2 Effect of Rayleigh number Ra

Velocity distribution

Figure 2 shows how the velocity field in the vented enclosure changes as Ra increases from 10^3 to 10^7 at fixed $O = 0.5$, $S = 0.5$, and $\varepsilon = 0.5$. At low Ra (10^3) the flow is weak and conduction-dominated, forming small symmetric recirculation cells. Through the moderate range $(10^4 - 10^5)$ natural convection sets in, the velocity rises modestly, and organized circulation zones develop as fluid is exchanged vertically through the apertures. At the transitional value (10^6), convection accelerates, resulting in the formation of a vertical plume above C_R, hence enhancing the buoyancy-driven motion. At high Ra (10^7) the flow is well organized and energetic: a high-velocity thermal plume rises above C_R and carries the peak velocities of the field, cold air enters through the lower aperture, and warm fluid leaves through the upper one. The flow is asymmetric, a direct result of the buoyancy of C_R, and surface radiation at $\varepsilon = 0.5$ moderates the temperature gradients at low Ra while its influence fades as Ra rises. The flow therefore shifts from a conduction-controlled to a convection-controlled regime as Ra increases, which sustains ventilation and improves heat removal through the apertures.

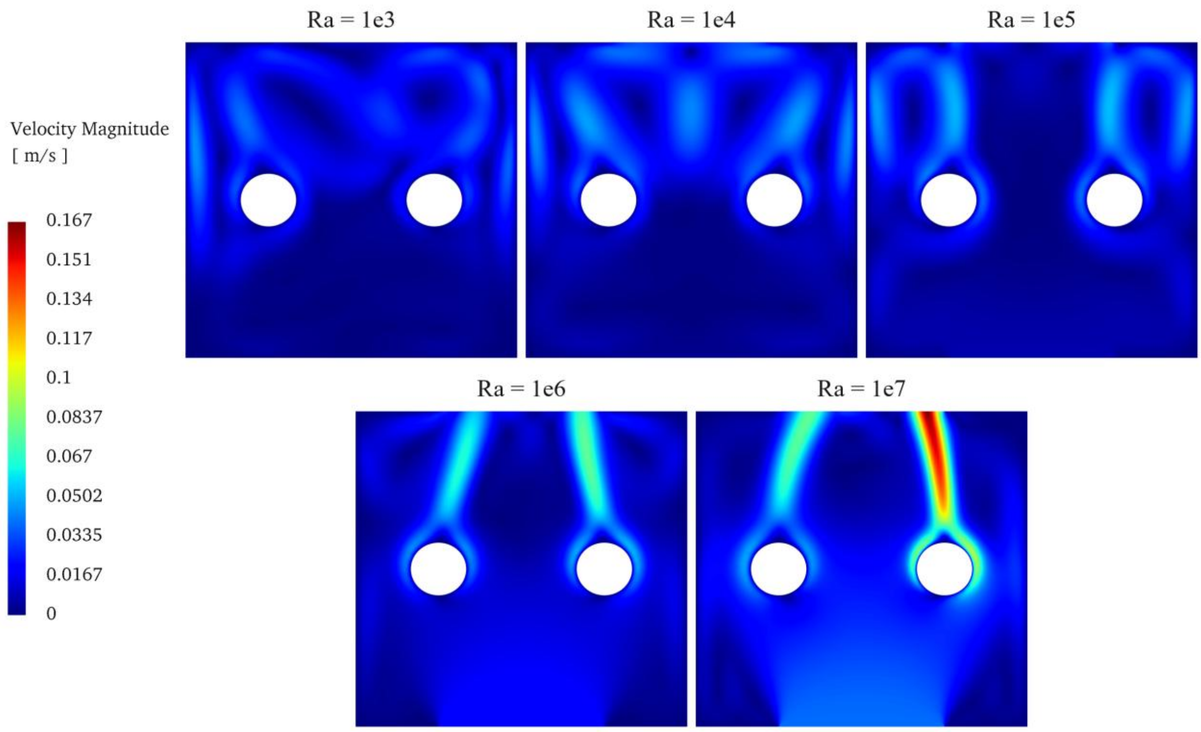

Figure (2): Velocity-magnitude contours over the Ra sweep ($Ra = 10^3 - 10^7$) at $O = 0.5$, $S = 0.5$, $\varepsilon = 0.5$.

Temperature distribution

Figure 3 illustrates the static-temperature field over the same Ra range, at the same fixed $O = 0.5$, $S = 0.5$, and $\varepsilon = 0.5$. At $Ra = 10^3$, where conduction dominates, the temperature is almost uniform, with weak gradients and negligible fluid motion. Between $Ra = 10^4$ and 10^5 convection begins: sharper gradients appear next to the cylinders and the thermal boundary layers thin, marking the onset of buoyancy and a slight upward drift. At $Ra = 10^6$ convection prevails, a thermal plume forms above C_R, the isotherms are compressed, and the temperature field becomes asymmetric under buoyancy. At $Ra = 10^7$ convection is fully developed: the plume rises strongly, steep gradients surround C_R, and effective ventilation leaves a cooler core, while the air around C_L warms only slightly. Surface radiation at $\varepsilon = 0.5$ lowers the peak temperatures and softens the gradients at low Ra, but becomes unimportant once convection dominates at higher Ra. Heat transfer thus moves from conduction to convection as Ra increases, the isotherms changing from nearly uniform to plume-driven and the cavity's heat-removal efficiency improving accordingly.

Heat transfer characteristics

Figure 4 traces Nu_{Conv} and Nu_{Rad} of C_L and C_R against Ra at fixed $O = 0.5$, $S = 0.5$, and $\varepsilon = 0.5$. At $Ra = 10^3$, Nu_{Conv} of C_L exceeds that of C_R (4.8 against 4.5); the two curves converge at $Ra = 10^4$ (both ≈ 5.1), and C_R overtakes C_L for every $Ra \geq 10^5$, reaching 7.41 against 6.69 at $Ra = 10^7$. This crossover reflects the growing role of C_R's own buoyancy: at low Ra the two cylinders are only weakly differentiated and conduction dominates around both bodies nearly symmetrically, but as Ra increases the larger driving temperature difference at C_R produces an increasingly vigorous plume (Fig. 2) that thins its local boundary layer and lifts its convective coefficient above that of the passively cooled C_L. Nu_{Rad} falls with Ra on both cylinders, from about 5.5 at low Ra to 3.5 (C_L) and 4.3 (C_R) at $Ra = 10^7$: since radiative exchange is set mainly by the surface-to-ambient temperature level rather than by Ra, it stays comparatively flat while the convective coefficient grows with the strengthening buoyant flow, so radiation's relative share of the total shrinks as Ra rises. The same qualitative Ra-dependence, radiation dominant at low Ra and increasingly overtaken by convection at high Ra, was reported by Ali and Mahmood [4] for a single radiating cylinder in an otherwise similar vented enclosure, where the total-Nu enhancement attributable to radiation fell from 70–300% at low Ra to 25–125% at high Ra; the present results extend that trend to a differentially heated pair. Because the rising convective and falling radiative contributions nearly compensate, the total $Nu_{Tot} = Nu_{Conv} + Nu_{Rad}$ stays close to 10.2–10.3 on both cylinders for $Ra \leq 10^6$; only at $Ra = 10^7$ does Nu_{Tot} of C_R climb to 11.7, against 10.2 for C_L, as convection outpaces the radiative decline. Conduction and radiation therefore govern the low-Ra regime, while convection takes over at high Ra, most strongly for C_R.

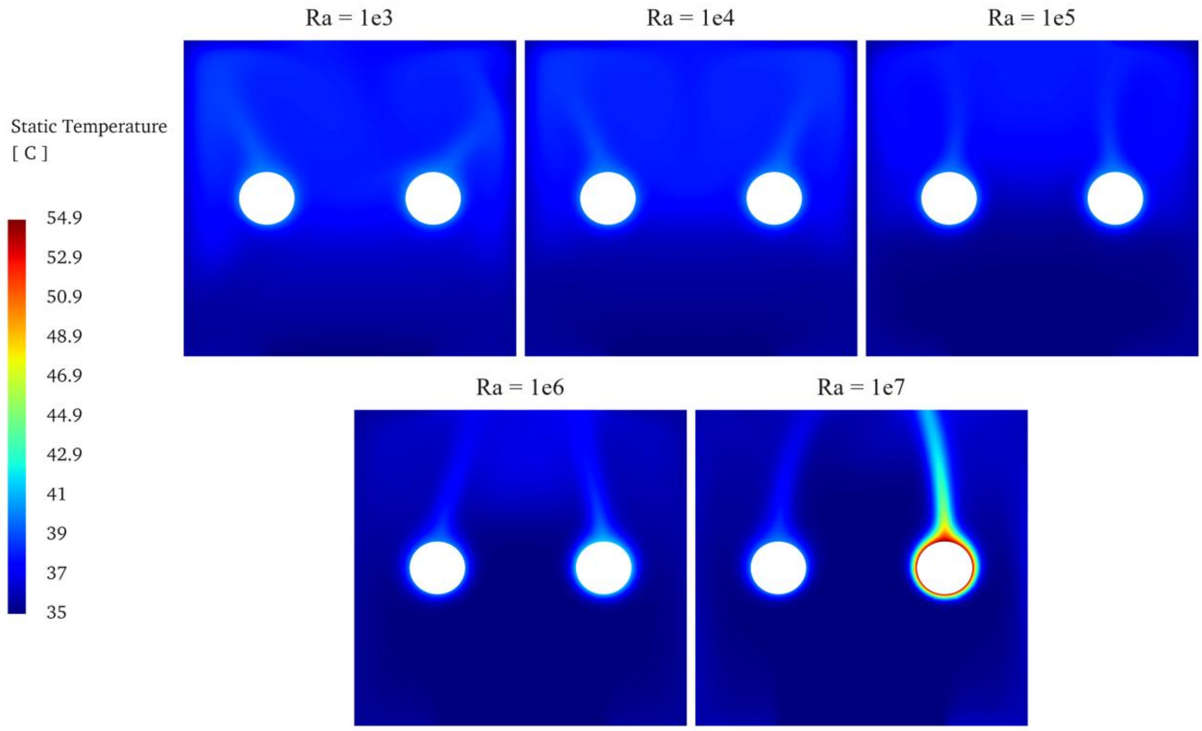

Figure (3): Static-temperature contours over the Ra sweep ($Ra = 10^3 - 10^7$) at $O = 0.5$, $S = 0.5$, $\varepsilon = 0.5$.

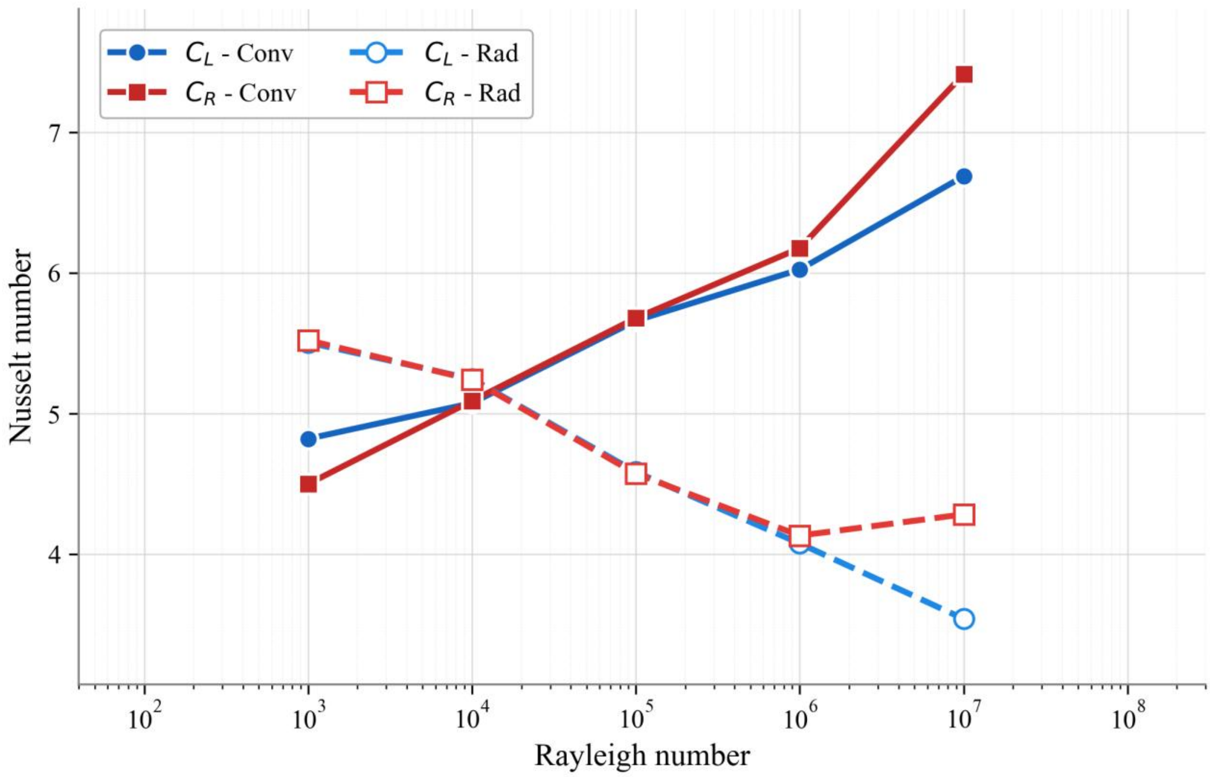

Figure (4): Nu_{Conv} and Nu_{Rad} versus Ra for C_L and C_R at $O = 0.5$, $S = 0.5$, $\varepsilon = 0.5$.

3.3 Effect of opening ratio O

Velocity distribution

Figure 5 depicts the velocity field for O from 0.05 to 1 at fixed $Ra = 3.37 \times 10^6$, $S = 0.5$, and $\varepsilon = 0.5$. At $O = 0.05$ the flow is weak: recirculation raises the velocity near the upper orifice while the thermal plumes stay confined. As O widens to 0.25, ascending streams and vertical jets appear, though recirculation persists. At $O = 0.5$ strong vertical plumes develop and entrain more air. At $O = 0.75$ a chimney-like flow forms, with forceful jets and reduced recirculation; the jet strength and pattern change only slightly on widening further to $O = 1$. This plateau reflects the buoyancy-driven pressure head, which is set by Ra (held fixed in this sweep) and does not grow with the vent area: once the opening is wide enough that entrance and exit losses no longer limit the flow, further widening chiefly increases the mass flow rate through the larger cross-section rather than the peak jet velocity, consistent with the heat-transfer results below, where Nu_{Conv} peaks near $O \approx 0.75$ and eases slightly at $O = 1$ rather than continuing to rise. A similar interior optimum, rather than a monotonic trend, was reported by Alomar et al. [27] for a differentially heated cylinder pair in the same enclosure family, where the maximum Nusselt number occurred at an intermediate opening ($O = 0.439$) rather than at their widest tested value. For C_L, the flow develops from minimal recirculation at $O = 0.05$, through stronger entrainment and pronounced interaction with the C_R plume at $O = 0.25 - 0.5$, to near-independence from C_R at $O = 0.75 - 1$, where it draws cooler air locally. The flow therefore changes from recirculation-dominated to plume-driven as O widens, which improves air exchange and heat-transfer efficiency at both cylinders up to the point where the vent ceases to be the limiting resistance.

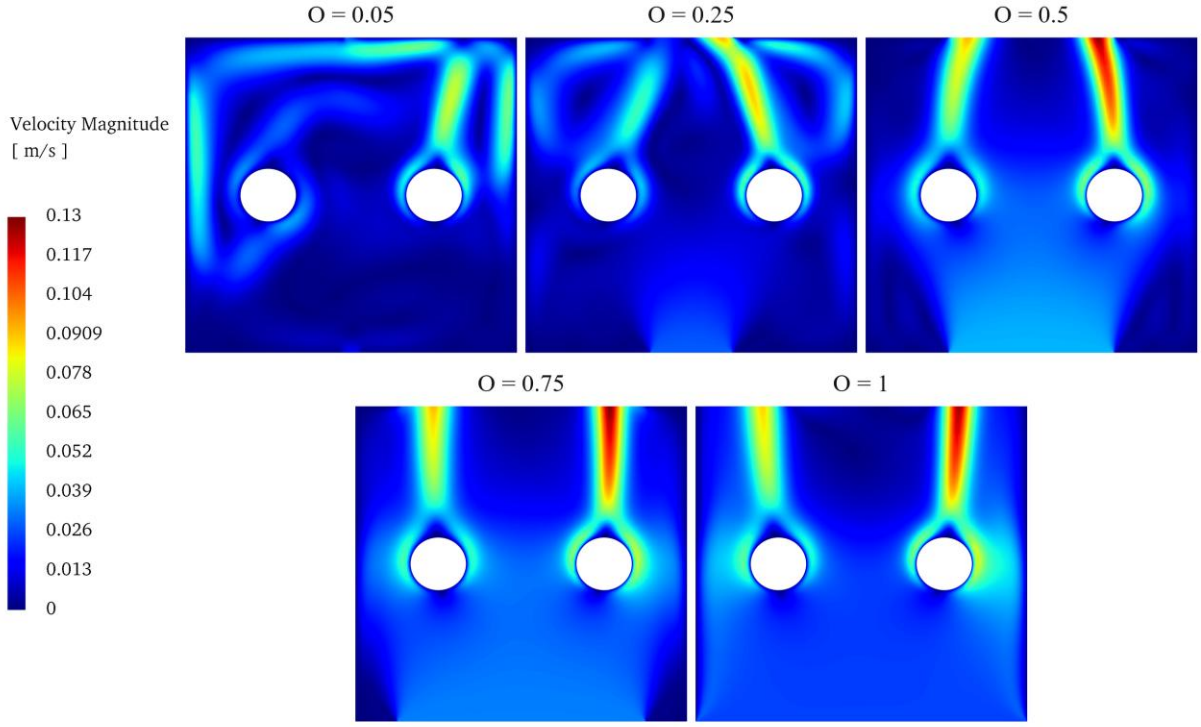

Figure (5): Velocity-magnitude contours over the O sweep ($O = 0.05 - 1.0$) at $Ra = 3.37 \times 10^6$, $S = 0.5$, $\varepsilon = 0.5$.

Temperature distribution

Figure 6 reports the static-temperature field as O increases from 0.05 to 1 at fixed $Ra = 3.37 \times 10^6$, $S = 0.5$, and $\varepsilon = 0.5$. At $O = 0.05$ the cavity is thermally stratified, dominated by warm fluid with little cold inflow. As O widens toward 0.25 only weak cooling occurs and the thermal plumes remain concentrated. At $O = 0.5$ a clear thermal plume forms, cooling improves, and the field shifts toward convection. At $O = 0.75$ heat is dissipated efficiently and the thermal boundary layers thin, while at $O = 1$ vertical plume transport gives near-uniform cooling and limits heat build-up. C_R drives this buoyant flow, which turns from diffuse to jet-like as O grows. The coupling between C_L and C_R varies with O: strong at $O = 0.05$, partial at $O = 0.5$, and effectively independent at $O \geq 0.75$, where separate vertical flow paths form. The temperature field thus changes from diffusion-dominated to plume-driven, most clearly for $O \geq 0.75$, which improves cooling and reduces thermal stratification inside the enclosure.

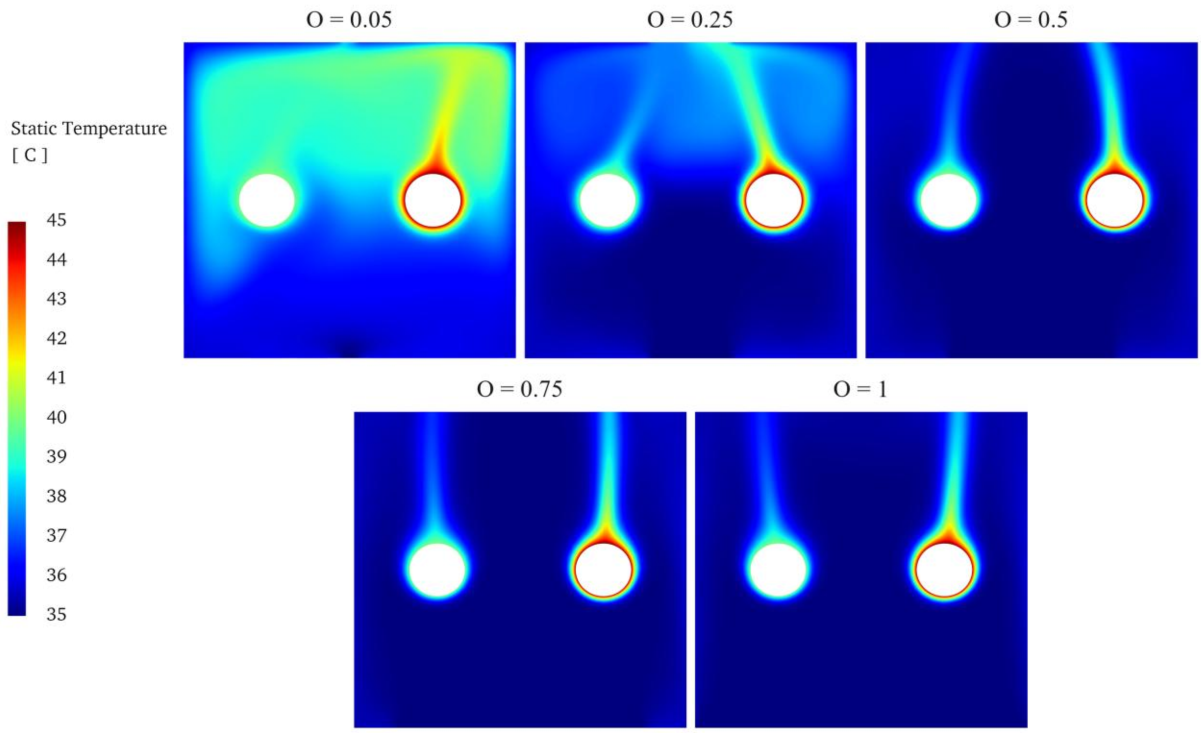

Figure (6): Static-temperature contours over the O sweep ($O = 0.05 - 1.0$) at $Ra = 3.37 \times 10^6$, $S = 0.5$, $\varepsilon = 0.5$.

Heat transfer characteristics

Figure 7 shows Nu_{Conv} and Nu_{Rad} of C_L and C_R across O from 0.05 to 1 at fixed $Ra = 3.37 \times 10^6$, $S = 0.5$, and $\varepsilon = 0.5$. Nu_{Conv} of C_L starts at 5.5, peaks at 6.4 near $O \approx 0.75$, and eases to 6.33 at $O = 1$. C_R starts at 5.9, peaks at 6.82 near $O \approx 0.75$, and eases to 6.8. Larger O therefore improves ventilation and buoyancy, peaking Nu_{Conv} near $O = 0.75$. Nu_{Rad} falls as O widens: C_L drops from about 6.8 to 4.0, and C_R from about 5.05 to a near-constant 4.15. Small O favors radiation and large O favors convection, because both Nusselt numbers are referred to the difference between the cylinder surface and the enclosure air, and only the convective heat rate is proportional to that difference. At $O = 0.05$ the hot air discharged by the cylinders cannot leave the cavity, so the enclosure air temperature rises and that difference becomes small. The convective heat rate falls with it and Nu_{Conv} changes little, while the radiative heat rate is set by the surface temperatures of the cylinders and the walls and is almost unaffected, so Nu_{Rad} becomes large. As O widens the cavity is ventilated, the enclosure air returns toward the inlet temperature, and the same driving difference is restored, which raises Nu_{Conv} and lowers Nu_{Rad}. C_R keeps the higher Nu_{Conv} throughout, and the dominant mode shifts from radiation to convection, with the best performance near $O = 0.75$. At small O the system therefore operates in a mixed mode with substantial radiative exchange, whereas at large O it shifts to a convection-dominated regime, consistent with the extensive hot regions at low O and the slender thermal plumes at high O seen in the temperature contours. The opposing convective rise and radiative fall nearly cancel once the vent is wide, so the total Nu_{Tot} of C_L is highest at the tightest opening, reaching 12.3 at $O = 0.05$, about 19% above the 10.3–10.4 plateau it holds for $O \geq 0.25$; the hot air trapped at $O = 0.05$ (Fig. 6) raises the radiative share enough to dominate the total.

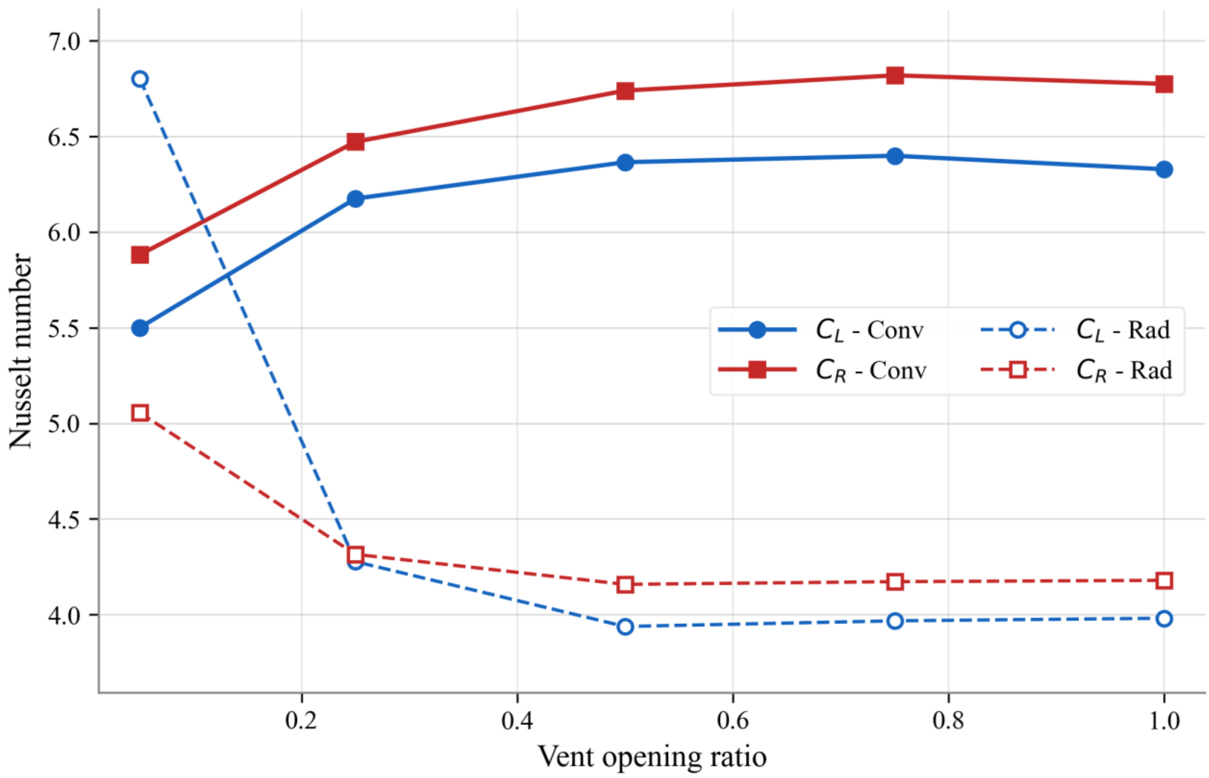

Figure (7): Nu_{Conv} and Nu_{Rad} versus O for C_L and C_R at $Ra = 3.37 \times 10^6$, $S = 0.5$, $\varepsilon = 0.5$.

3.4 Effect of spacing ratio S

Velocity distribution

Figure 8 traces the velocity field as S varies from 0.25 to 0.75 at fixed $Ra = 3.37 \times 10^6$, $O = 0.5$, and $\varepsilon = 0.5$. At small S (0.25), the interaction is strong and the thermal plumes merge into a dominant central jet: the narrow inter-cylinder gap acts as a nozzle that accelerates the upward flow between C_L and C_R. As S widens to $0.35 - 0.5$, the plumes partly separate and behave semi-independently. At intermediate-to-large S (0.65), distinct vertical jets form with little interaction, and at large S (0.75), the plumes become independent and the efficiency around C_L falls. Wider S therefore moves the flow from merged jets to separate plumes, improving its organization and stability. Close S promotes mixing but introduces instability, moderate S balances stability against useful interaction, and wide S lets C_R's plume develop without interference from C_L, though this undisturbed development does not translate into a higher Nusselt number for either cylinder, as the heat-transfer results below show. S thus exerts a strong influence on the flow, shifting it from an interaction-dominated to a plume-dominated regime as the cylinders separate.

Temperature distribution

Figure 9 presents the temperature field as S varies from 0.25 to 0.75 at fixed $Ra = 3.37 \times 10^6$, $O = 0.5$, and $\varepsilon = 0.5$. At small S (0.25), the same nozzle effect that accelerates the flow between the cylinders (Fig. 8) also raises the local fluid temperature in the gap through combined convective and radiative heating, so C_L sits in a warmer local environment than at wider spacing. As S rises to $0.35 - 0.5$, the plumes begin to separate and this inter-cylinder heating weakens. At $S \geq 0.65$, the two plumes develop largely independently near the cylinders themselves, but they bend back toward one another and partially recombine before leaving the enclosure (visible in the $S = 0.65$ and $S = 0.75$ panels), because the top vent is fixed in width and position and does not widen or shift with the cylinder spacing; mass conservation through that single fixed opening still forces the two plumes to reconverge downstream. Greater S thus reduces thermal contact between the cylinders near the bodies themselves, and gives the lowest local temperature around C_L, even though the fixed-vent geometry still couples their plumes further downstream. This local cooling of C_L at wide S does not by itself imply higher heat transfer, since the same nozzle effect that warms the gap at small S also raises the local convective coefficient there, as the Nusselt-number results below show.

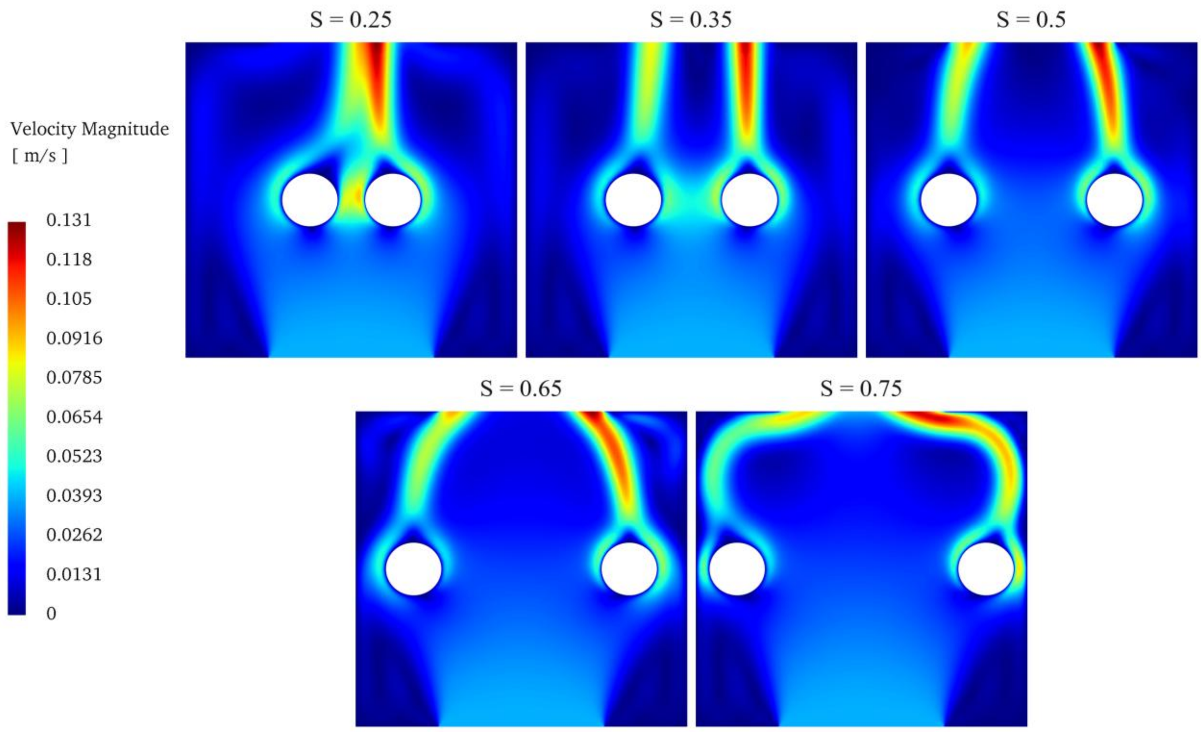

Figure (8): Velocity-magnitude contours over the S sweep ($S = 0.25 - 0.75$) at $Ra = 3.37 \times 10^6$, $O = 0.5$, $\varepsilon = 0.5$.

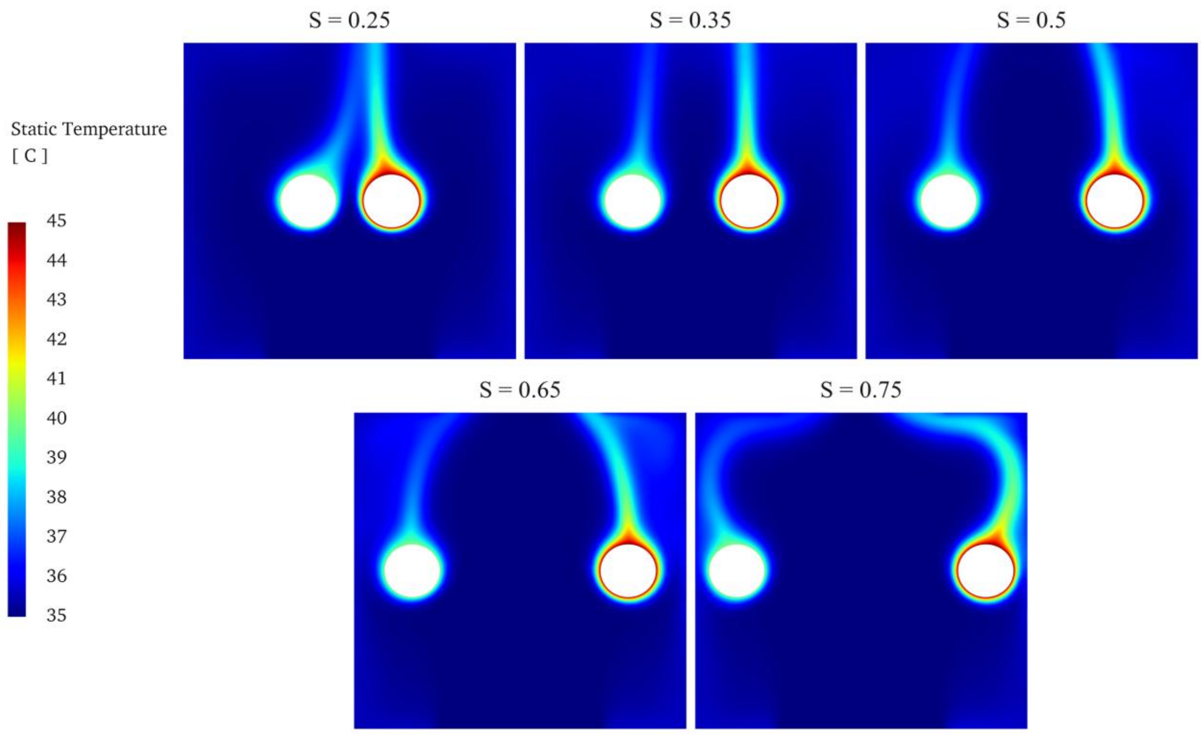

Figure (9): Static-temperature contours over the S sweep ($S = 0.25 - 0.75$) at $Ra = 3.37 \times 10^6$, $O = 0.5$, $\varepsilon = 0.5$.

Heat transfer characteristics

Figure 10 illustrates Nu_{Conv} and Nu_{Rad} of C_L and C_R for S from 0.25 to 0.75 at fixed $Ra = 3.37 \times 10^6$, $O = 0.5$, and $\varepsilon = 0.5$. C_R keeps higher Nu values than C_L, and convection exceeds radiation for both. As S increases, Nu_{Conv} of C_L falls from 6.67 to 6.12 and that of C_R falls from 7.0 to about 6.65–6.70: the nozzle-accelerated flow at small S thins the local boundary layer on the facing sides of both cylinders and raises their convective coefficient, an effect that weakens as the gap widens and the inter-cylinder flow decelerates. Nu_{Rad} of C_L rises from 3.62 at $S = 0.25$ to a maximum of 3.95 near $S \approx 0.65$ before declining to 3.75 at $S = 0.75$, and C_R follows the same pattern. This interior maximum reflects two competing view-factor effects as S changes: closer spacing raises the mutual radiative exchange between C_L and C_R, but at the smallest S each cylinder increasingly shadows the other's view of the wider, cooler enclosure and limits the net radiative loss, so the balance between these effects peaks at a moderate separation. Summed over both modes, Nu_{Tot} of C_R falls from 11.1 at $S = 0.25$ to 10.7 at $S = 0.75$, and that of C_L from 10.3 to 9.9, so wider spacing lowers the total for both cylinders. Close S therefore strengthens the coupling and improves convective heat transfer specifically, while radiative transfer is maximized at a moderate, intermediate spacing. The same spacing sensitivity appears in the natural-convection measurements of Alomar et al. [27], a differentially heated cylinder pair in the same enclosure family, in which the highest Nusselt number occurred at the smallest tested spacing ($S = 0.351$); it contrasts with the uniformly heated pair of Ali [12], where Nu instead rises with S, a difference consistent with the present nozzle mechanism depending on the temperature contrast between C_L and C_R, which is absent when both cylinders are held at the same temperature.

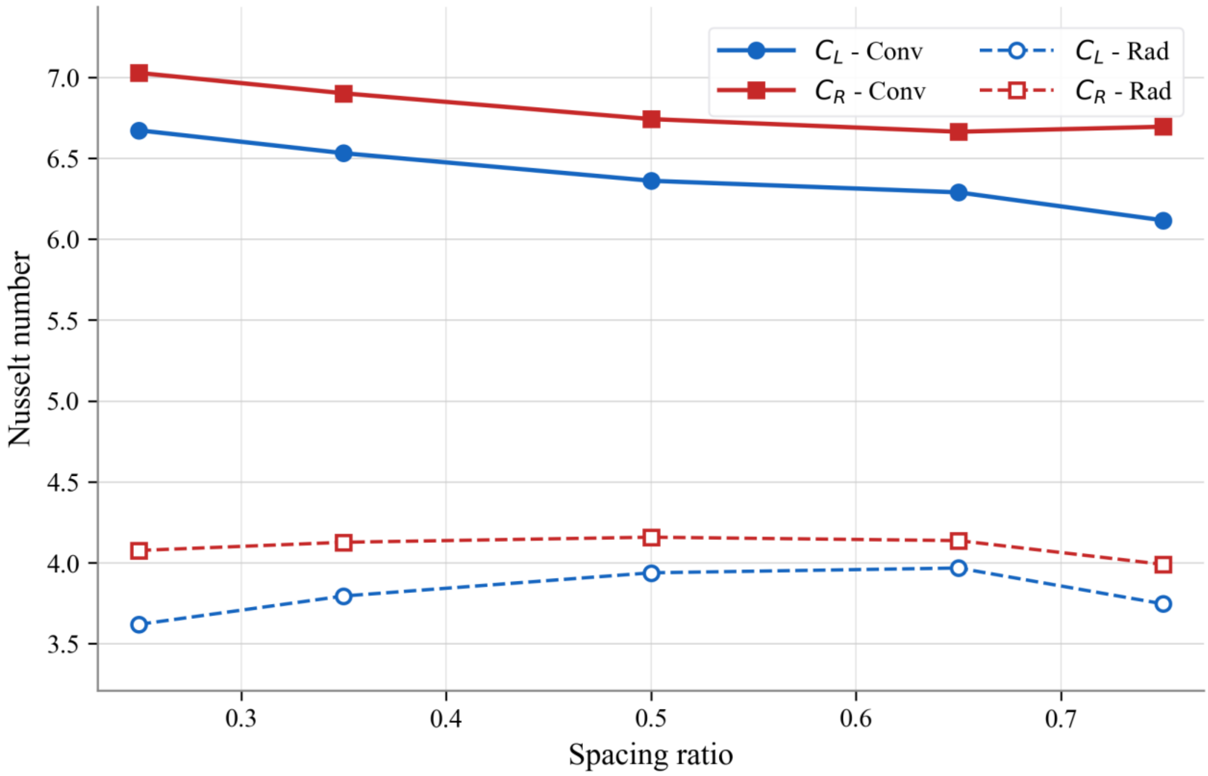

Figure (10): Nu_{Conv} and Nu_{Rad} versus S for C_L and C_R at $Ra = 3.37 \times 10^6$, $O = 0.5$, $\varepsilon = 0.5$.

3.5 Effect of cylinders emissivity ε

Velocity distribution

Figure 11 shows the velocity-magnitude contours over the ε sweep at fixed $Ra = 3.37 \times 10^6$, $O = 0.5$, and $S = 0.5$. The buoyancy-driven flow is largely insensitive to ε: a thin, intense plume rises above C_R at $\varepsilon = 0$, and its shape and peak velocity change only marginally as ε increases to 1. This near-invariance is consistent with the heat-transfer results below, in which the convective Nusselt number is almost independent of ε; radiation adds a parallel transfer path without materially altering the velocity field that convection establishes.

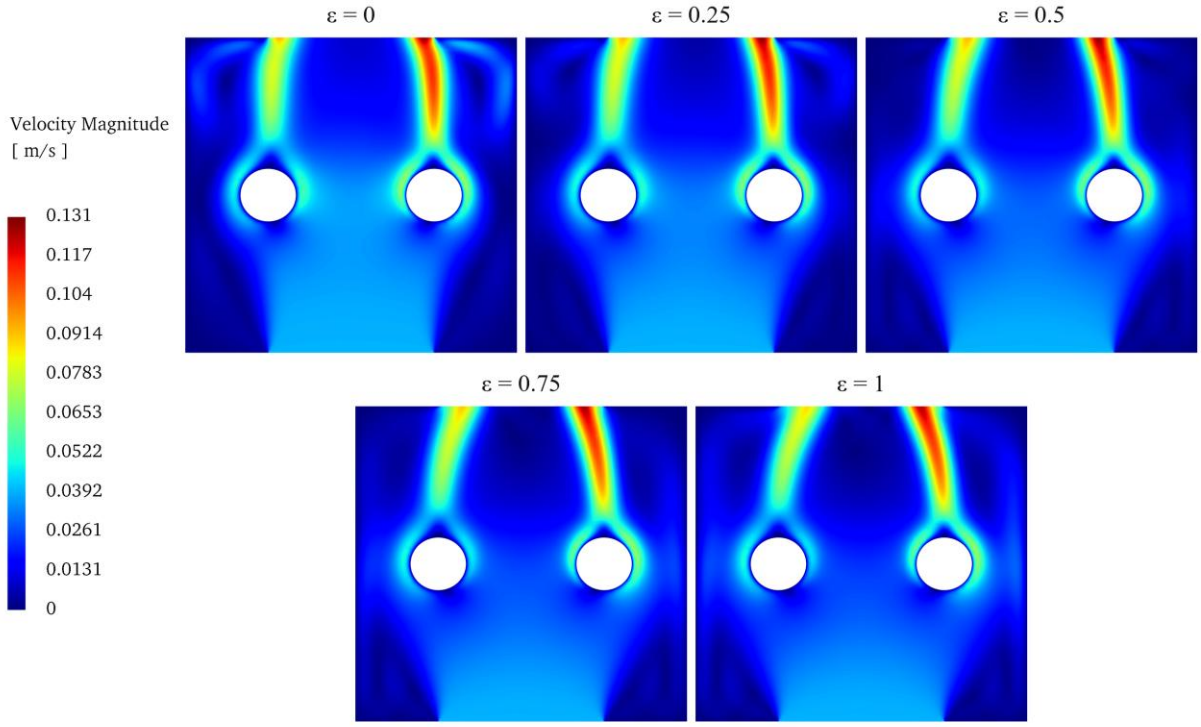

Figure (11): Velocity-magnitude contours over the ε sweep ($\varepsilon = 0 - 1.0$) at $Ra = 3.37 \times 10^6$, $O = 0.5$, $S = 0.5$.

Temperature distribution

Figure 12 represents the impact of emissivity variation on the temperature distribution at fixed $Ra = 3.37 \times 10^6$, $O = 0.5$, and $S = 0.5$. As ε increases from 0 to 1, the interaction between the two cylinders transitions from being mostly governed by convection to demonstrating significant convection–radiation coupling. At low emissivity ($\varepsilon = 0$–0.25), heat transfer is predominantly governed by natural convection, the plume is slender, and the thermal contact between the two cylinders is negligible. As emissivity rises ($\varepsilon = 0.25$–0.75), radiative exchange enhances the thermal coupling, the temperature around C_L rises, and the plume broadens. At high emissivity ($\varepsilon = 0.75$–1.0), radiation dominates and the field becomes more uniform with gentle gradients, as the view-factor-coupled exchange raises the temperature near C_L and reduces the gradients adjacent to C_R.

The temperature field therefore responds visibly to ε, while the velocity field of Fig. 11 stays nearly invariant. Radiation acts directly on the surface and near-wall temperatures through view-factor exchange, so its signature appears first in the temperature field. Its effect on the flow is only indirect, through the resulting change in buoyancy, and that effect stays small because Ra is held fixed across the sweep.

Heat transfer characteristics

Figure 13 traces Nu_{Conv} and Nu_{Rad} against ε at fixed $Ra = 3.37 \times 10^6$, $O = 0.5$, and $S = 0.5$. Nu_{Conv} changes little on C_L and C_R; it falls from 6.5 to 6.4 on C_L and from 6.9 to 6.7 on C_R. Raising ε increases radiation but has little effect on the buoyancy-driven flow. Nu_{Rad} rises almost linearly with ε, reaching 6.9 for C_L and 8.0 for C_R, so radiation dominates at high ε. Heat transfer changes from purely convective at $\varepsilon = 0$ to a convective–radiative combination as ε rises. The radiative share of C_L grows from 0 to 52% of the total, with C_R following the same trend to 54%. As ε rises, the near-constant convective contribution is increasingly outweighed by the growing radiative one, shifting the balance toward radiation dominance. Nu_{Tot} increases by about 105% for C_L and 113% for C_R as ε rises from 0 to 1. This near-independence of Nu_{Conv} from ε differs from the sealed-cavity results of Hamimid and Guellal [32], Ridouane et al. [30], Singh and Singh [36], and Sadripour et al. [35], in which the convective Nusselt number falls as emissivity rises. The difference is consistent with the through-flow of the present vented configuration: cooler make-up air drawn continuously through the lower vent replaces the near-wall fluid and buffers the thermal boundary layer against the wall-temperature rise that radiation produces, whereas in a sealed cavity the radiatively warmed fluid cannot leave and the convective coefficient is depressed. The mechanism is advanced as a hypothesis consistent with the present fields rather than a proven cause.

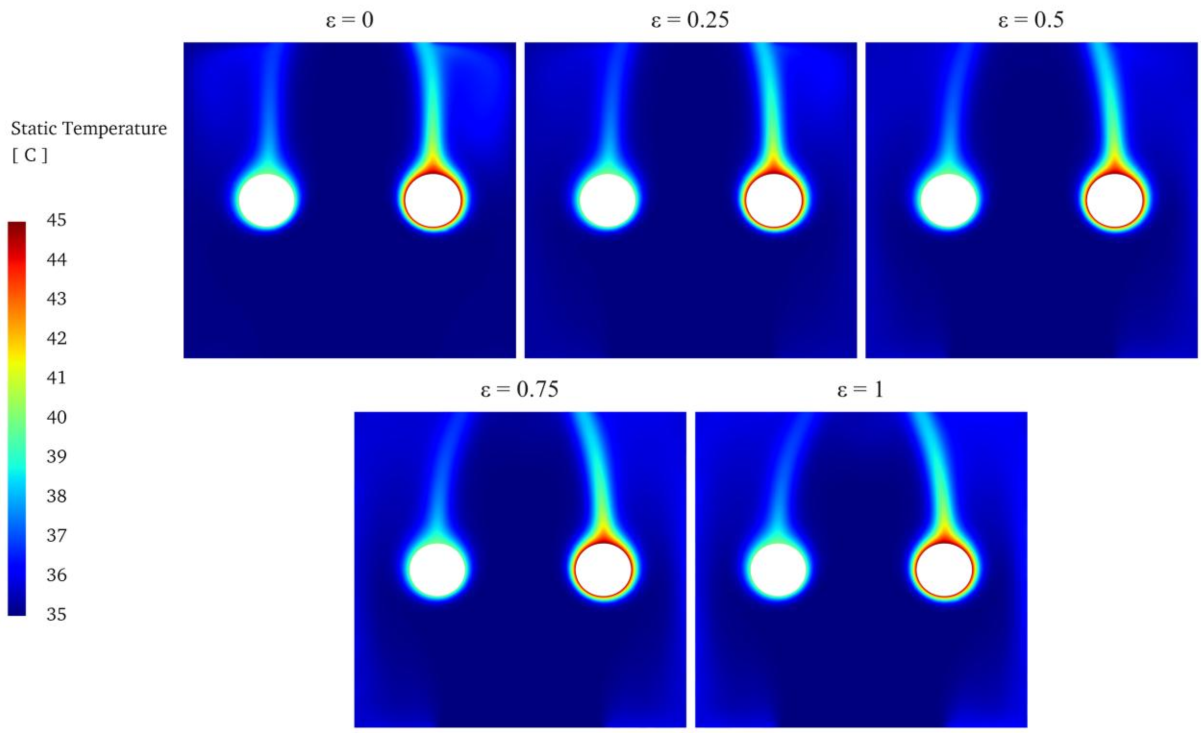

Figure (12): Static-temperature contours over the ε sweep ($\varepsilon = 0 - 1.0$) at $Ra = 3.37 \times 10^6$, $O = 0.5$, $S = 0.5$.

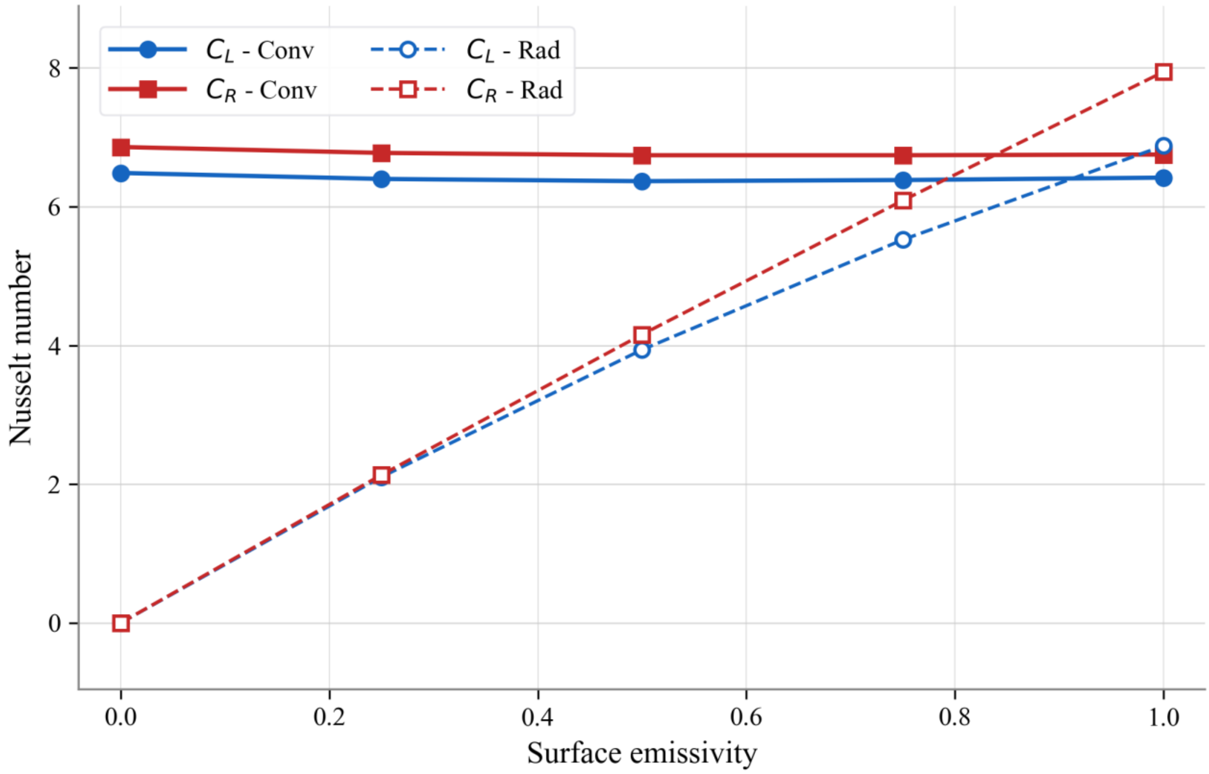

Figure (13): Nu_{Conv} and Nu_{Rad} versus ε for C_L and C_R at $Ra = 3.37 \times 10^6$, $O = 0.5$, $S = 0.5$.

Figure 14 reports the Q_{Conv} and Q_{Rad} contributions to the heat transfer of C_L and C_R as ε changes, at fixed $Ra = 3.37 \times 10^6$, $O = 0.5$, and $S = 0.5$. At $\varepsilon = 0$ heat is transferred entirely by convection. As ε rises to 0.25, radiation accounts for about 25% of the transfer. At $\varepsilon = 0.5$ the radiative share rises to about 38%, and at $\varepsilon = 0.75$ radiation nearly matches convection at about $46 - 47\%$. At $\varepsilon = 1$ radiation dominates, contributing about $52 - 54\%$. The balance therefore shifts clearly from convection-dominated to radiation-dominated heat transfer as ε increases.

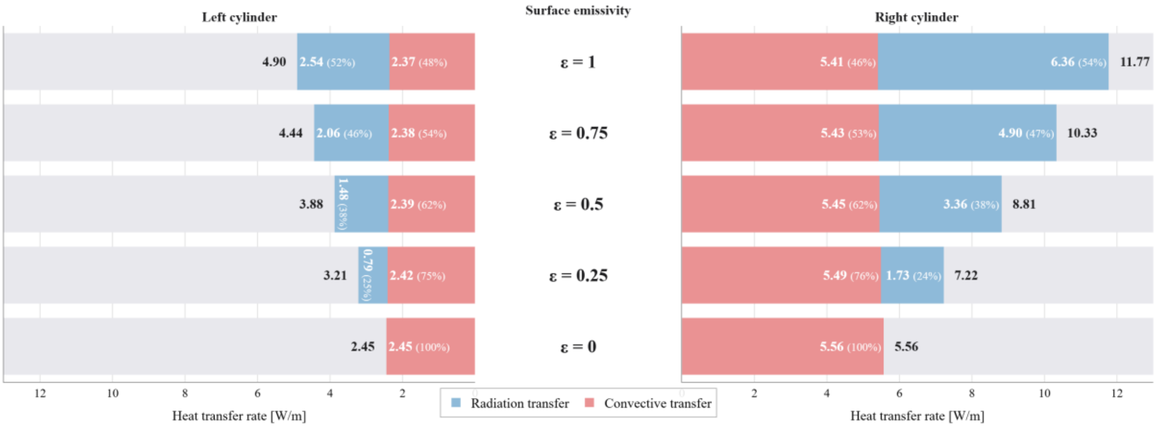

Figure (14): Stacked-bar decomposition of Q_{Conv} and Q_{Rad} for C_L and C_R, in W/m, against ε at $Ra = 3.37 \times 10^6$, $O = 0.5$, $S = 0.5$.

4. Conclusions

Combined natural convection and surface-to-surface radiation heat transfer from two horizontally aligned cylinders, C_L and C_R, in a vented square enclosure has been examined numerically. The actions of Ra, ε, O, and S on Nu_{Conv}, Nu_{Rad}, and Nu_{Tot} of C_L and C_R, and on the convective–radiative partition of the wall heat transfer, have been presented and discussed. Comparison against 18 experimental cases gives a mean error of 4.6% and a maximum of 7.0%. The following conclusions are drawn:

1. The average fluid temperature inside the enclosure is governed by O and S through the mass flow rate. At $O = 0.05$ the discharged hot air is trapped and the fluid temperature rises well above ambient, whereas at larger O the cavity is ventilated and the fluid temperature approaches ambient. At $S = 0.25$ the flow accelerates through the gap in a nozzle-like manner and raises the inter-cylinder fluid temperature, and this nozzle effect decays as S increases.

2. The total Nusselt number of C_L and C_R remains nearly constant, between 10.2 and 10.3, for $10^3 \leq Ra \leq 10^6$, because the rising convective contribution and the falling radiative contribution nearly compensate as Ra increases. Nu_{Conv} of C_R overtakes that of C_L from $Ra = 10^5$ onwards and reaches 7.41 at $Ra = 10^7$, while Nu_{Rad} falls from about 5.5 to 3.5–4.3. At $Ra = 10^7$, Nu_{Tot} of C_R increases sharply to 11.7 while that of C_L remains near 10.2; the more vigorous plume of C_R recirculates warm air over C_L and suppresses its heat transfer, so the interaction between C_L and C_R is asymmetric.

3. The opening ratio O has a strong influence on Nu_{Tot} at small O only. Nu_{Tot} of C_L reaches 12.3 at $O = 0.05$, about 19% above its plateau value of 10.3–10.4, because the trapped hot air raises the average fluid temperature and reduces the driving temperature difference on which Nu_{Tot} is based; C_L is affected more than C_R. At $O = 0.25$ the ventilation is sufficient to remove this effect, after which Nu_{Tot} is insensitive to further increase in O. The convective coefficient peaks near $O = 0.75$ as ventilation improves and then eases once the vent is no longer the limiting resistance.

4. The spacing ratio S has a considerable influence on Nu_{Tot} for both cylinders. Nu_{Tot} decreases as S increases, for C_R from 11.1 at $S = 0.25$ to 10.7 at $S = 0.75$, because the nozzle-accelerated flow between the cylinders, which thins the boundary layer on their facing sides, weakens as they are separated. At $S = 0.75$, C_L decouples from C_R and its Nu_{Tot} drops to 9.9.

5. The cylinder emissivity ε has the largest influence on heat transfer. As ε increases from 0 to 1, Nu_{Tot} rises by about 105% for C_L (from 6.5 to 13.3) and about 113% for C_R (from 6.9 to 14.7), while the convective contribution decreases by less than 3.5%. Radiation therefore acts as a heat-transfer path additional to convection and roughly doubles Nu_{Tot}.

6. The radiative contribution accounts for 38% of the total heat transfer at $\varepsilon = 0.5$ and becomes the dominant mode, between 52% and 54%, at $\varepsilon = 1$. A convection-only model therefore under-predicts total heat transfer by between 38% and 54%, and the S2S model is essential for an accurate prediction of the combined-mode heat transfer.

Acknowledgements

No financial support was received for this research.

Conflict of Interest

The authors declare that they have no known competing financial interests or personal relationships that could have appeared to influence the work reported in this paper.

Nomenclature

Latin symbols

Symbol	Description	Unit
c_p	Specific heat capacity of air	J/(kg·K)
C_L	Left cylinder	–
C_R	Right cylinder	–
D	Cylinder diameter	m
D_r	Cylinder diameter ratio	–
E	Comparison error	%
F_{ij}	View factor	–
g, g_i	Gravitational acceleration	m/s²
G_k	Turbulent kinetic energy production	kg/(m·s³)
Y_k	Turbulent kinetic energy dissipation	kg/(m·s³)
G_b	Buoyancy production of turbulent kinetic energy	kg/(m·s³)
G_ω	Specific dissipation rate production	kg/(m³·s²)
Y_ω	Specific dissipation rate destruction	kg/(m³·s²)
$G_{\omega b}$	Buoyancy production of specific dissipation rate	kg/(m³·s²)
D_ω	Cross-diffusion term	kg/(m³·s²)
Gr	Grashof number	–
h_{ext}	External convection coefficient	W/(m²·K)
J_i, J_j	Radiosity	W/m²
k	Turbulent kinetic energy	m²/s²
$k_{acrylic}$	Thermal conductivity of acrylic	W/(m·K)
k_f	Thermal conductivity of air	W/(m·K)
L	Enclosure side length	m
N	Number of radiating surfaces	–
Nu	Nusselt number	–
$\overline{Nu}$	Pair-averaged Nusselt number, the mean over C_L and C_R	–
$\overline{Nu}_{avg}$	Pair-averaged Nusselt number	–
$\overline{Nu}_{CFD}$	Predicted pair-averaged Nusselt number	–
$\overline{Nu}_{exp}$	Experimental pair-averaged Nusselt number	–
Nu_{C_L}	Area-averaged Nusselt number on C_L	–
Nu_{C_R}	Area-averaged Nusselt number on C_R	–
Nu_{Conv}	Area-averaged convective Nusselt number	–
Nu_{Rad}	Area-averaged radiative Nusselt number	–
Nu_{Tot}	Area-averaged total Nusselt number	–

Symbol	Description	Unit
o	Vent opening width	m
O	Opening ratio, o/L	–
P	Pressure	Pa
P_{gauge}	Outlet gauge pressure	Pa
Pr	Prandtl number	–
Pr_t	Turbulent Prandtl number	–
q''	Surface heat flux	W/m²
q''_{Conv}	Convective surface heat flux	W/m²
q''_{Rad}	Radiative surface heat flux	W/m²
q''_{wall}	Wall heat flux	W/m²
$\nabla \cdot q_{Rad}$	Volumetric radiative source term	W/m³
Q_{Conv}	Convective heat transfer rate	W/m
Q_{Rad}	Radiative heat transfer rate	W/m
Ra	Rayleigh number	–
Re	Reynolds number	–
Ri	Richardson number	–
s	Cylinder center-to-center spacing	m
S	Spacing ratio, s/L	–
T	Temperature	K
T_{avg}	Volume-averaged air temperature	K
T_{in}	Wall interior face temperature	K
T_{out}	Wall exterior face temperature	K
T_i	Temperature of radiating surface i	K
T_s	Cylinder surface temperature	K
T_L	Surface temperature of C_L	K
T_R	Surface temperature of C_R	K
T_{ref}	Reference temperature	K
u_i, u_j	Velocity components	m/s
U_{inlet}	Inlet velocity magnitude	m/s
W_z	Spanwise duct depth	m
x_i, x_j	Cartesian coordinate directions	m
y	Vertical Cartesian coordinate	m
y^+	Dimensionless wall distance	–
Δx	Enclosure wall thickness	m

Greek symbols

Symbol	Description	Unit
α	Thermal diffusivity of air	m²/s
β	Thermal expansion coefficient of air	1/K
ΔT	Cylinder surface temperature difference	K
ε	Surface emissivity	–
ε_c	Cylinder surface emissivity	–

Symbol	Description	Unit
ε_{ext}	Exterior wall emissivity	–
ε_i	Radiating surface emissivity	–
μ	Dynamic viscosity of air	Pa·s
μ_t	Turbulent viscosity	Pa·s
ν	Kinematic viscosity of air	m^2/s
ρ	Density of air	kg/m^3
ρ_0	Reference density	kg/m^3
ρ_i	Surface reflectivity	–
σ	Stefan–Boltzmann constant	$W/(m^2 \cdot K^4)$
σ_k	Closure coefficient for k	–
σ_ω	Closure coefficient for ω	–
τ	Optical thickness	–
ω	Specific dissipation rate	1/s

References

1. S. R. Pradhan, V. M. Behera, S. K. Rathore, and J. R. Senapati, “Study of combined effect of natural convection and radiation heat transfer from annular finned vertical cylinder,” Heat Transfer, vol. 52, no. 2, pp. 1754–1777, 2023, doi: https://doi.org/10.1002/htj.22762.
2. R. S. Prasad, S. N. Singh, and A. K. Gupta, “A systematic approach for optimal positioning of heated side walls in a side vented open cavity under natural convection and surface radiation,” Frontiers in Heat and Mass Transfer, vol. 11, Art. no. 15, 2018a, doi: https://doi.org/10.5098/hmt.11.15.
3. R. S. Prasad, S. N. Singh, and A. K. Gupta, “Coupled laminar natural convection and surface radiation in partially right-side open cavities,” Frontiers in Heat and Mass Transfer, vol. 11, Art. no. 28, 2018b, doi: https://doi.org/10.5098/hmt.11.28.
4. O. M. Ali and R. A. Mahmood, “Effect of radiation on natural convection heat transfer from heated horizontal cylinder in vented enclosure,” IOP Conference Series: Materials Science and Engineering, vol. 978, no. 1, Art. no. 012030, 2020, doi: https://doi.org/10.1088/1757-899X/978/1/012030.
5. A. W. Kandeal, M. Ismail, A. Basem, M. M. Elsayad, W. H. Alawee, H. S. Majdi, A. S. Abdullah, S.-H. Jang, M. An, Z. M. Omara, N. M. Ghazaly, and S. W. Sharshir, “An overview of the improvement of natural convection heat transfer via surface thermal radiation for different geometries,” Results in Engineering, vol. 23, Art. no. 102514, 2024, doi: https://doi.org/10.1016/j.rineng.2024.102514.
6. A. Andreozzi and O. Manca, “Radiation effects on natural convection in a vertical channel with an auxiliary plate,” International Journal of Thermal Sciences, vol. 97, pp. 41–55, 2015, doi: https://doi.org/10.1016/j.ijthermalsci.2015.05.013.
7. E. Yu and Y. K. Joshi, “Air cooling of a vented enclosure by combined conduction, natural convection and radiation,” in Heat transfer: Volume 2 — Heat transfer in turbulent flows; Fundamentals of convection heat transfer; Fundamentals of natural convection in laminar and turbulent flows; Natural circulation, ASME, 1996, pp. 323–330, doi: https://doi.org/10.1115/IMECE1996-0083.
8. L. C. Ngo, T. Bello-Ochende, and J. P. Meyer, “Numerical modelling and optimisation of natural convection heat loss suppression in a solar cavity receiver with plate fins,” Renewable Energy, vol. 74, pp. 95–105, 2015, doi: https://doi.org/10.1016/j.renene.2014.07.047.
9. M. Montiel González, J. F. Hinojosa, and C. A. Estrada, “Numerical study of heat transfer by natural convection and surface thermal radiation in an open cavity receiver,” Solar Energy, vol. 86, no. 4, pp. 1118–1128, 2012, doi: https://doi.org/10.1016/j.solener.2012.01.005.
10. A. Castell, C. Solé, M. Medrano, J. Roca, L. F. Cabeza, and D. García, “Natural convection heat transfer coefficients in phase change material (PCM) modules with external vertical fins,” Applied Thermal Engineering, vol. 28, no. 13, pp. 1676–1686, 2008, doi: https://doi.org/10.1016/j.applthermaleng.2007.11.004.
11. A. Tamayol, F. McGregor, and M. Bahrami, “Thermal assessment of naturally cooled electronic enclosures with rectangular fins,” Journal of Electronic Packaging, vol. 134, no. 3, Art. no. 034501, 2012, doi: https://doi.org/10.1115/1.4007077.
12. O. M. Ali, “Effect of horizontal spacing on natural convection heat transfer from two aligned horizontal cylinders in a vented enclosure,” Arabian Journal for Science and Engineering, vol. 47, no. 10, pp. 8257–8272, 2022, doi: https://doi.org/10.1007/s13369-021-06259-2.
13. F. Karimi, H. Xu, Z. Wang, M. Yang, and Y. Zhang, “Numerical simulation of steady mixed convection around two heated circular cylinders in a square enclosure,” Heat Transfer Engineering, vol. 37, no. 1, pp. 64–75, 2016, doi: https://doi.org/10.1080/01457632.2015.1042343.
14. G. G. Gubareff, J. E. Janssen, and R. H. Torborg, Thermal radiation properties survey: A review of the literature, 2nd ed., Minneapolis-Honeywell Regulator Company, 1960.

15. F. Selimefendigil and H. F. Öztop, "Thermoelectric generation from vented cavities with a rotating conic object and highly conductive CNT nanofluids for renewable energy systems," International Communications in Heat and Mass Transfer, vol. 122, Art. no. 105139, 2021, doi: https://doi.org/10.1016/j.icheatmasstransfer.2021.105139.
16. O. M. Ali, R. A. Mahmood, and M. W. Al-Brifkani, "Augmentation of convection heat transfer from a horizontal cylinder in a vented square enclosure with variation of lower opening size," Thermal Science, vol. 26, no. 3A, pp. 2027–2041, 2022, doi: https://doi.org/10.2298/TSCI201119176A.
17. A. J. Chamkha, S. H. Hussain, and Q. R. Abd-Amer, "Mixed convection heat transfer of air inside a square vented cavity with a heated horizontal square cylinder," Numerical Heat Transfer, Part A: Applications, vol. 59, no. 1, pp. 58–79, 2011, doi: https://doi.org/10.1080/10407782.2011.541216.
18. M. M. Rahman, M. A. Alim, S. Saha, and M. K. Chowdhury, "Mixed convection in a vented square cavity with a heat-conducting horizontal solid circular cylinder," Journal of Naval Architecture and Marine Engineering, vol. 5, no. 2, pp. 37–46, 2008, doi: https://doi.org/10.3329/jname.v5i2.2504.
19. O. M. Ali and O. R. Alomar, "Mixed convection heat transfer from two aligned horizontal heated cylinders in a vented square enclosure," Thermal Science and Engineering Progress, vol. 25, Art. no. 101041, 2021, doi: https://doi.org/10.1016/j.tsep.2021.101041.
20. G. Y. Kahwaji, A. S. Hussien, and O. M. Ali, "Numerical investigation of natural convection heat transfer from square cylinder in a vented enclosure," Applied Mechanics and Materials, vol. 110–116, pp. 4451–4464, 2012, doi: https://doi.org/10.4028/www.scientific.net/AMM.110-116.4451.
21. O. R. Alomar, R. H. Saaeed, and O. M. Ali, "Impact of size and location of outflow opening vent on mixed convective heat transfer induced by two aligned heated cylinders immersed in a partially open channel," Heat Transfer, vol. 52, no. 4, pp. 3187–3226, 2023, doi: https://doi.org/10.1002/htj.22823.
22. M. H. Ali and R. E. Jalal, "Natural convection in a square enclosure with different openings and involves two cylinders: A numerical approach," Frontiers in Heat and Mass Transfer, vol. 15, Art. no. 27, 2020, doi: https://doi.org/10.5098/hmt.15.27.
23. F. Karimi, H. T. Xu, Z. Wang, M. Yang, and Y. Zhang, "Numerical simulation of unsteady natural convection from heated horizontal circular cylinders in a square enclosure," Numerical Heat Transfer, Part A: Applications, vol. 65, no. 8, pp. 715–731, 2014, doi: https://doi.org/10.1080/10407782.2013.846607.
24. H. W. Cho, Y. M. Seo, G. S. Mun, M. Y. Ha, and Y. G. Park, "The effect of instability flow for two-dimensional natural convection in a square enclosure with different arrays of two inner cylinders," International Journal of Heat and Mass Transfer, vol. 114, pp. 307–317, 2017, doi: https://doi.org/10.1016/j.ijheatmasstransfer.2017.06.080.
25. A. A. Yousif, O. M. Ali, D. Sadiq, O. R. Alomar, Q. S. Sabri, and A. M. Mohammed, "Effect of CuO-water nanofluid on natural convection from heated cylinders in a duct," Results in Engineering, vol. 27, Art. no. 106189, 2025, doi: https://doi.org/10.1016/j.rineng.2025.106189.
26. S. O. O. Al-Omar and O. M. Ali, "Mixed convection from two horizontally aligned hot and cold circular cylinders in a vented square enclosure," Ain Shams Engineering Journal, vol. 14, no. 8, Art. no. 102048, 2023, doi: https://doi.org/10.1016/j.asej.2022.102048.
27. O. R. Alomar, O. M. Ali, and S. O. O. Al-Omar, "Free convective heat transfer induced inside a vented duct having two aligned hot and cold cylinders: An experimental study," Heat Transfer, vol. 53, no. 6, pp. 3212–3234, 2024, doi: https://doi.org/10.1002/htj.23067.
28. Y. G. Park, H. S. Yoon, and M. Y. Ha, "Natural convection in square enclosure with hot and cold cylinders at different vertical locations," International Journal of Heat and Mass Transfer, vol. 55, no. 25–26, pp. 7911–7925, 2012, doi: https://doi.org/10.1016/j.ijheatmasstransfer.2012.08.012.
29. H. Sun, E. Chénier, and G. Lauriat, "Effect of surface radiation on the breakdown of steady natural convection flows in a square, air-filled cavity containing a centered inner body," Applied Thermal Engineering, vol. 31, no. 6–7, pp. 1252–1262, 2011, doi: https://doi.org/10.1016/j.applthermaleng.2010.12.028.
30. E. H. Ridouane, M. Hasnaoui, and A. Campo, "Effects of surface radiation on natural convection in a Rayleigh–Bénard square enclosure: Steady and unsteady conditions," Heat and Mass Transfer, vol. 42, no. 3, pp. 214–225, 2006, doi: https://doi.org/10.1007/s00231-005-0012-7.
31. J. F. Hinojosa, C. A. Estrada, R. E. Cabanillas, and G. Alvarez, "Numerical study of transient and steady-state natural convection and surface thermal radiation in a horizontal square open cavity," Numerical Heat Transfer, Part A: Applications, vol. 48, no. 2, pp. 179–196, 2005, doi: https://doi.org/10.1080/10407780590948936.
32. S. Hamimid and M. Guellal, "Numerical study of combined natural convection-surface radiation in a square cavity," Fluid Dynamics & Materials Processing, vol. 10, no. 3, pp. 377–393, 2014, doi: https://doi.org/10.3970/fdmp.2014.010.377.
33. G. V. Kuznetsov and A. E. Nee, "Conduction, convection, and radiation in a closed cavity with a local radiant heater," Frontiers in Heat and Mass Transfer, vol. 10, Art. no. 26, 2018, doi: https://doi.org/10.5098/hmt.10.26.
34. D. Sadaoui, A. Sahi, A. Djerrada, and K. Mansouri, "Coupled radiation and natural convection within an inclined sinusoidal solar collector heated from below," Mechanics & Industry, vol. 17, no. 3, Art. no. 302, 2016, doi: https://doi.org/10.1051/meca/2015060.
35. S. Sadripour, S. A. Ghorashi, and M. Estajloo, "Numerical investigation of a corrugated heat source cavity: A full convection-conduction-radiation coupling," American Journal of Aerospace Engineering, vol. 4, no. 3, pp. 27–37, 2017, doi: https://doi.org/10.11648/j.ajae.20170403.11.
36. D. K. Singh and S. N. Singh, "Conjugate free convection with surface radiation in open top cavity," International Journal of Heat and Mass Transfer, vol. 89, pp. 444–453, 2015, doi: https://doi.org/10.1016/j.ijheatmasstransfer.2015.05.038.
37. D. Gerich and H. Eckelmann, "Influence of end plates and free ends on the shedding frequency of circular cylinders," Journal of Fluid Mechanics, vol. 122, pp. 109–121, 1982, doi: https://doi.org/10.1017/S0022112082002110.

38. M. M. Zdravkovich, Flow around circular cylinders, vol. 1, Oxford University Press, 1997.
39. D. D. Gray and A. Giorgini, "The validity of the Boussinesq approximation for liquids and gases," International Journal of Heat and Mass Transfer, vol. 19, no. 5, pp. 545–551, 1976, doi: https://doi.org/10.1016/0017-9310(76)90168-X.
40. H. K. Versteeg and W. Malalasekera, An introduction to computational fluid dynamics: The finite volume method, 2nd ed., Pearson Education, 2007.
41. F. R. Menter, "Two-equation eddy-viscosity turbulence models for engineering applications," AIAA Journal, vol. 32, no. 8, pp. 1598–1605, 1994, doi: https://doi.org/10.2514/3.12149.
42. D. C. Wilcox, Turbulence modeling for CFD, 2nd ed., DCW Industries, 1998.
43. R. Siegel and J. R. Howell, Thermal radiation heat transfer, 4th ed., Taylor & Francis, 2001.